

Optimal interpolation-based coordinate descent method for parameterized quantum circuits

Zhijian Lai¹, Jiang Hu², Taehee Ko³, Jiayuan Wu⁴, and Dong An¹

¹Beijing International Center for Mathematical Research, Peking University, Beijing 100871, People's Republic of China

²Department of Mathematics, University of California, Berkeley, Berkeley, CA 94720, USA

³School of Computational Sciences, Korea Institute for Advanced Study, Seoul 02455, South Korea

⁴Wharton Department of Statistics and Data Science, University of Pennsylvania, Philadelphia, PA 19104, USA

Parameterized quantum circuits appear ubiquitously in the design of many quantum algorithms, such as variational quantum algorithms, where the optimization of parameters is crucial for algorithmic efficiency. In this work, we propose an Optimal Interpolation-based Coordinate Descent (OICD) method to solve the parameter optimization problem that arises in parameterized quantum circuits. Our OICD method employs an interpolation technique to approximate the cost function of a parameterized quantum circuit, effectively recovering its trigonometric characteristics, then performs an argmin update on a single parameter per iteration on a classical computer. We determine the optimal interpolation nodes in our OICD method to mitigate the impact of statistical errors from quantum measurements. Additionally, for the case of equidistant frequencies — commonly encountered when the Hermitian generators are Pauli operators — we show that the optimal interpolation nodes are equidistant nodes, and our OICD method can simultaneously minimize the mean squared error, the condition number of the interpolation matrix, and the average variance of derivatives of the cost function. We perform numerical simulations of our OICD method using Qiskit Aer and test its performance on the maxcut problem, the transverse field Ising model, and the XXZ model. Numerical results imply that our OICD method is more efficient than the commonly used stochastic gradient descent method and the existing random coordinate descent method.

1 Introduction

Variational quantum algorithms (VQAs) [1, 2] are a class of hybrid quantum-classical algorithms designed for certain optimization problems. VQAs make use of the advantages of quantum systems while handling the challenges of noisy hardware, making them well-suited for solving complicated computational problems in the near future. VQAs have been applied across a wide range of fields. For example, in quantum physics and quantum chemistry, the variational quantum eigensolver (VQE) has been used to calculate ground-state energies [3, 4, 5, 6] and simulate the dynamics of quantum systems [7, 8, 9]. The quantum approximate optimization algorithm (QAOA) has shown promise in addressing combinatorial optimization problems [10, 11, 12]. In addition, VQAs play a central role in quantum machine learning, enabling advancements in tasks such as classification, regression, and generative modeling [13, 14, 15, 16, 17, 18]. These applications underscore the broad impact of VQAs on the practical domains.

Zhijian Lai: lai_zhijian@pku.edu.cn, <https://galvinlai.github.io/>

Jiang Hu: jianghu@berkeley.edu, <https://hujiangpku.github.io/>

Taehee Ko: kthmomo@kias.re.kr, <https://sites.google.com/view/taeheeko>

Jiayuan Wu: jiyuanw@wharton.upenn.edu

Dong An: dongan@pku.edu.cn, <https://dong-an.github.io/>

The VQA framework operates on a hybrid quantum-classical paradigm. The quantum part involves parameterized quantum circuits (PQCs), which are controlled by the tunable classical parameters. By executing these circuits and performing measurements on quantum devices, a cost function is evaluated, representing the quality of the current solution. This cost function is then fed into a classical optimization algorithm, which updates the current parameters to improve the outcome. Specifically, in this work, we consider a q -qubit quantum system with $N := 2^q$. Finding the parameters in PQCs ultimately leads us to solve the following unconstrained optimization problem:

$$\min_{\boldsymbol{\theta} \in \mathbb{R}^m} f(\boldsymbol{\theta}) = \langle 0|U(\boldsymbol{\theta})^\dagger M U(\boldsymbol{\theta})|0\rangle. \quad (1)$$

Here, $U(\boldsymbol{\theta}) \in \mathbb{C}^{N \times N}$ is a PQC that depends on a set of classical parameters $\boldsymbol{\theta} = [\theta_1, \theta_2, \dots, \theta_m]^\dagger \in \mathbb{R}^m$. Typically, the circuit $U(\boldsymbol{\theta})$ is applied to a fixed and easily prepared initial state $|0\rangle \in \mathbb{C}^N$, yielding the output state $U(\boldsymbol{\theta})|0\rangle$ in a quantum device. In the context of quantum mechanics, $f(\boldsymbol{\theta})$ is precisely the expectation value of the Hermitian observable $M \in \mathbb{C}^{N \times N}$, measured with respect to that output state. As in many studies [19, 20, 21, 22], we consider the typical PQC structure as

$$U(\boldsymbol{\theta}) = V_m U_m(\theta_m) \cdots V_1 U_1(\theta_1), \quad (2)$$

where V_j are fixed arbitrary gates, and $U_j(\theta_j)$ are rotation-like gates, defined as

$$U_j(\theta_j) = e^{iH_j\theta_j}, \quad j = 1, \dots, m, \quad (3)$$

for some Hermitian generators $H_j \in \mathbb{C}^{N \times N}$. Notice that each U_j is a single-parameter gate and fully captures the dependence on univariate $\theta_j \in \mathbb{R}$.

In the paradigm of VQAs, the classical optimization techniques play a crucial role. Initially, derivative-free optimization methods (such as Nelder-Mead, differential evolution) were commonly used to solve Eq. (1). However, *gradient-based* optimization methods have gained increasing popularity due to their significant advantages, including convergence guarantees [19, 22] and support from a wealth of mature algorithms, e.g., stochastic gradient descent (SGD) [19] and random coordinate descent (RCD) [22]. The so-called parameter-shift rule (PSR) [20, 21, 23] gives the unbiased estimation of derivatives by evaluating the cost function in Eq. (1) at the finite shifted parameter positions and combining those results linearly. This unbiased derivative estimation approach provides a solid foundation for various gradient-based optimization techniques. Specifically, SGD [19] method requires the full gradient $\nabla f(\boldsymbol{\theta})$ at each iteration, followed by an update to all parameters in the direction of $-\nabla f(\boldsymbol{\theta})$, scaled by a learning rate. RCD [22], on the other hand, randomly selects a single coordinate j at each iteration, computes the partial derivative $\partial_j f(\boldsymbol{\theta})$, and updates only that coordinate by $-\partial_j f(\boldsymbol{\theta})$, scaled by a learning rate.

For optimizing the parameters in PQCs, the main cost lies in the evaluation of the cost function, namely, the calling of $\boldsymbol{\theta} \mapsto f(\boldsymbol{\theta})$. This process is the only part of VQAs that relies on quantum device. Effective optimization techniques can achieve faster reductions of cost function with fewer function evaluations, thereby improving the efficiency of the whole VQAs. Thus, this paper primarily focuses on the classical algorithmic approach to solve Eq. (1). Since RCD only requires the computation of a single partial derivative, its numerical efficiency outperforms SGD.

In this work, we propose an optimal *interpolation-based* coordinate descent (OICD) to find the parameters in PQCs. Similar to RCD, our OICD method randomly selects and updates one parameter at each iteration. However, OICD update strategy is based on the following observation: according to [20], the dependence of cost function in Eq. (1) on single parameter, say θ_j , can be expressed as a finite Fourier series, represented as a linear combination of sine and cosine functions as

$$\theta_j \mapsto f(\boldsymbol{\theta}) = \frac{1}{\sqrt{2}} a_0 + \sum_{k=1}^{r_j} \left[a_k \cos\left(\Omega_k^j \theta_j\right) + b_k \sin\left(\Omega_k^j \theta_j\right) \right], \quad \text{fix other } m-1 \text{ parameters}, \quad (4)$$

where a_0, a_k and b_k are some unknown coefficients and constants r_j and $\{\Omega_k^j\}_{k=1}^{r_j}$ is fully determined by H_j corresponding to θ_j . We will give detail discussion for above expression in Section 2.2. We use the interpolation method to recover all the true Fourier coefficients a_0, a_k , and b_k as much as

possible. Once these estimated coefficients are obtained, existing solvers¹ on classical computers can be employed to minimize the function value with respect to the selected θ_j . The overall OICD process is shown in Fig. 1.

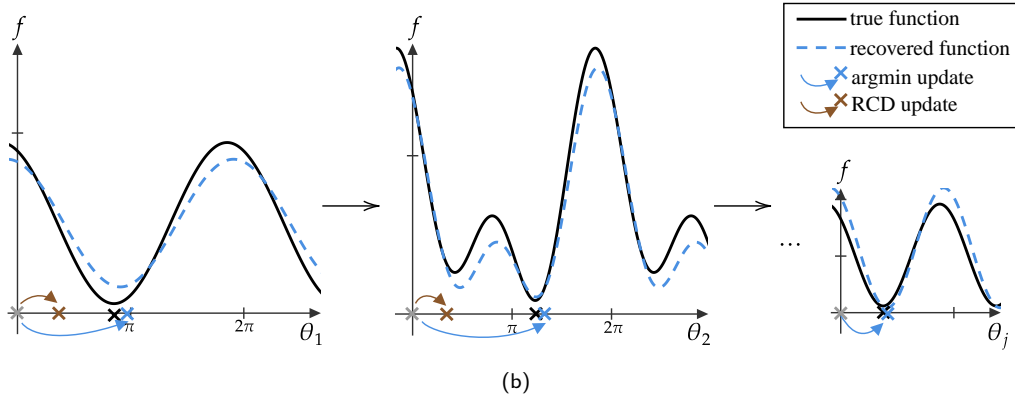
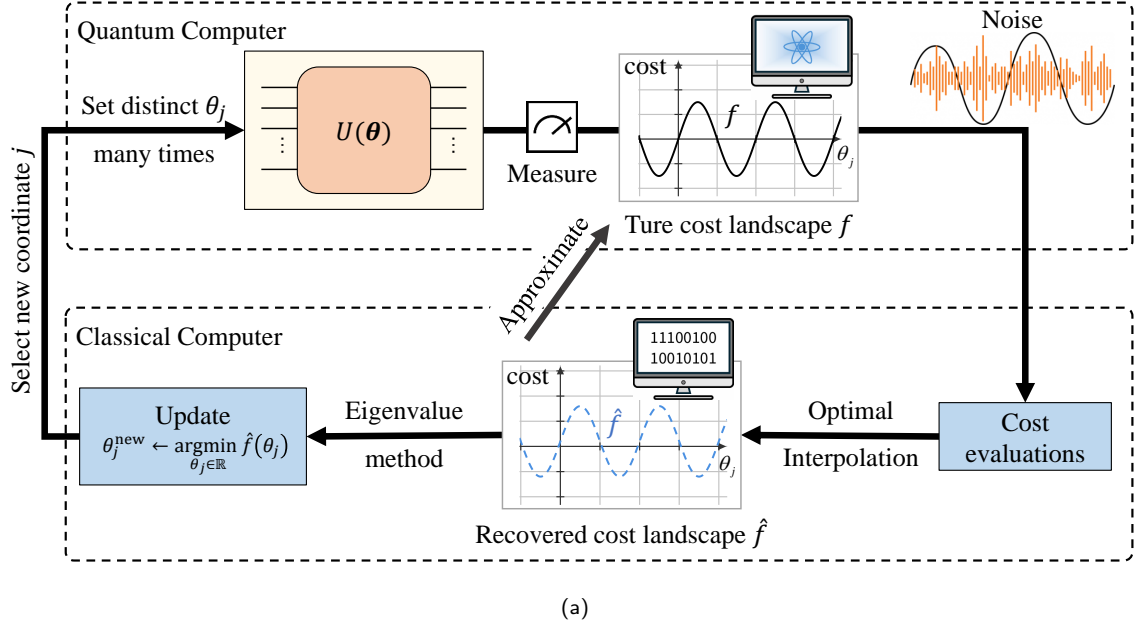


Figure 1: (a) A diagram illustrating the OICD algorithm workflow. (b) Suppose we first update θ_1 , then update θ_2 , and so on. We move the current value of θ_j (the gray cross) to the origin. The black solid line represents the true curve of f with respect to θ_j , and we aim to find the true minimum (the black cross). However, in PQCs, this black line is inherently non-usable because f is an expectation. By using an interpolation method under noisy conditions, we obtain relatively accurate estimates of a_0 , a_k , and b_k in Eq. (4). Using these estimated coefficients, we recover an approximate function, represented by the blue dashed line. This approximate function is fully usable, and its value at any point can be evaluated using classical computer. In each update step, OICD finds the global minimum of the approximate function (the blue cross), i.e., takes the argmin, which results in a significantly larger descent compared to the RCD method using one step update (the brown cross).

The interpolation method in our OICD has advantages similar to those of PSR, as it only requires finite function evaluations at some positions (called interpolation nodes) to reconstruct the original true function, without the need for additional ansatz. However, since the cost function is an expectation value, its exact values are generally unavailable, i.e., the function evaluations are inherently noisy due to at least the statistical errors. To this end, in our OICD method, we precompute an optimal set of interpolation nodes to minimize the impact of noise for each θ_j .

¹When $\Omega_k^j = k$, the eigenvalue method in Appendix F can solve it exactly.

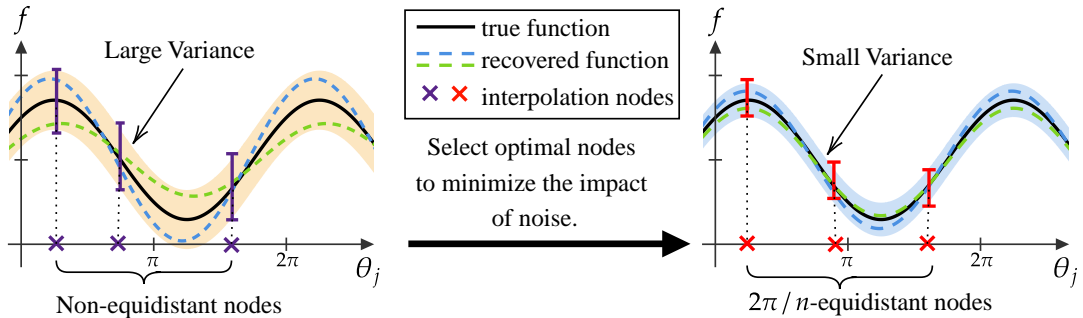


Figure 2: Variance between the approximate functions (recovered from different interpolation nodes) and the true function varies. Suppose we consider θ_j and theoretical true curve (black solid line) is $\theta_j \mapsto f(\theta) = a_0 + a_1 \cos(\theta_j) + b_1 \sin(\theta_j)$. To recover $n = 3$ values (a_0 , a_1 , and b_1), we simply select n different nodes, evaluate their corresponding f values, and solve a linear equation. The details of the interpolations will be given in Section 3. Since the f values always contain noise, the recovered function r_j only approximate the true function within a certain range. It can be proven that for any positive integer r_j and $\Omega_k^j = k$, the $2\pi/n$ -equidistant nodes are the optimal interpolation nodes, as they yield the closest approximation to the true function.

These optimal interpolation nodes are calculated only once and can be reused across subsequent iterations. The effects of different interpolation nodes are shown in Fig. 2. A detailed explanation will be provided in Section 3.

Table 1 summarizes the comparison of the number of function evaluations N_{eval} required per iteration for our OICD, as well as for SGD and RCD. This indicates that OICD and RCD require the same quantum resources, but OICD is interpolation-based method, while RCD is gradient-based method.

	SGD	RCD	OICD
N_{eval}	$2\ \mathbf{r}\ _1$	$2r_j$	$2r_j$

Table 1: Number of distinct circuit evaluations N_{eval} for single update. Here, $\|\mathbf{r}\|_1 = \sum_{j=1}^m r_j$ and integers r_j 's are the numbers of terms in the trigonometric expansion of the cost function given in Eq. (4), and will be formally introduced in Section 2.2 later.

Contribution The main contributions of this work can be summarized as follows.

1. We propose an optimal interpolation-based coordinate descent (OICD) method to address the parameter optimization problem in PQCs. By incorporating interpolation techniques, the OICD method significantly reduces reliance on quantum devices, thereby enhancing computational efficiency. This is because, in OICD, the evaluated function values are not directly used for computing gradients/partial derivatives but rather to reconstruct the entire landscape of the cost function on a classical computer as accurately as possible. In contrast, gradient-based methods like SGD and RCD use the evaluated function values directly to compute the gradients/partial derivatives at the current parameter, and the derivatives can only be used for a single update (requiring re-evaluation for subsequent updates). In OICD, however, the reconstructed function can be used for multiple updates using any optimization solvers, without additional quantum device operations, substantially reducing the quantum-related burden. In the numerical simulation, we test the maxcut problem, the transverse field Ising model (TFIM), and the XXZ problem, demonstrating that OICD is more effective than RCD and SGD.
2. For the case of equidistant frequencies (which is most common in PQCs, particularly when H_j in Eq. (3) are Pauli words), we have shown that using $\frac{2\pi}{n}$ -equidistant interpolation nodes is an optimal scheme. This specific scheme simultaneously satisfies the following three criteria: (1) minimization of the mean squared error between estimated Fourier coefficients and true coefficients, (2) minimization of the condition number of the interpolation matrix, and (3)

minimization of the average variance of the estimated derivatives. Moreover, we find that the subproblem of optimizing a single parameter in each iteration can be exactly solved by eigenvalue method proposed in [24]. We add it in Appendix F.

Organization This paper is organized as follows. In Section 2, we reformulate the cost function within the framework of optimization theory, offering a clear mathematical interpretation. In Section 3, we propose our OICD method for the general case where Hermitian H_j in the PQC can be arbitrary. In Section 4, we discuss the equidistant frequency case, which is the most common in practical applications, and demonstrate further theoretical advantages of our proposed OICD method. In Section 5, we discuss our numerical experiments, applying the OICD to the maxcut problem, the TFIM and the XXZ problem, and comparing our OICD with SGD and RCD. We conclude the paper in Section 6 with a summary of our work and potential future directions.

1.1 Notations

The superscript \dagger denotes the transpose for real matrices/vectors and the complex conjugate transpose for complex matrices/vectors. We use $\text{VAR}[\cdot]$ to denote the covariance matrix of a random vector, $\text{Var}[\cdot]$ to represent the variance of a random variable, and $\text{Cov}[\cdot, \cdot]$ to indicate the covariance between two random variables.

2 Restating the problem

In this section, we restate Eq. (1) from the perspective of optimization theory, providing its physical background in a precise mathematical context.

2.1 Setting I: statistical nature from quantum measurement postulate

According to the quantum measurement postulate [25], the cost function in Eq. (1) is the expected value of a discrete random variable Λ . For an observable corresponding to a Hermitian operator $M \in \mathbb{C}^{N \times N}$ with spectral decomposition $M = \sum_{m=1}^N \lambda_m P_m$, the probability of obtaining eigenvalue λ_m when measuring the state $|\psi(\boldsymbol{\theta})\rangle = U(\boldsymbol{\theta})|0\rangle$ is given by $p_{\boldsymbol{\theta}}(m) = \langle \psi(\boldsymbol{\theta}) | P_m | \psi(\boldsymbol{\theta}) \rangle \geq 0$, and the expectation of Λ is

$$\mathbb{E}_{\Lambda \sim p_{\boldsymbol{\theta}}}[\Lambda] = \langle \psi(\boldsymbol{\theta}) | M | \psi(\boldsymbol{\theta}) \rangle = f(\boldsymbol{\theta}). \quad (5)$$

The variance of Λ is

$$\text{Var}_{\Lambda \sim p_{\boldsymbol{\theta}}}[\Lambda] = \langle \psi(\boldsymbol{\theta}) | M^2 | \psi(\boldsymbol{\theta}) \rangle - [f(\boldsymbol{\theta})]^2 = \sigma^2(\boldsymbol{\theta}). \quad (6)$$

To estimate $f(\boldsymbol{\theta})$, we perform \mathbf{n} identical measurements (shots) and compute the sample mean $\bar{\Lambda} = \frac{1}{\mathbf{n}}(\Lambda_1 + \dots + \Lambda_{\mathbf{n}})$, where the Λ_i 's are i.i.d. samples from $p_{\boldsymbol{\theta}}$. We then have

$$\mathbb{E}_{\Lambda \sim p_{\boldsymbol{\theta}}}[\bar{\Lambda}] = f(\boldsymbol{\theta}), \quad \text{Var}_{\Lambda \sim p_{\boldsymbol{\theta}}}[\bar{\Lambda}] = \frac{\sigma^2(\boldsymbol{\theta})}{\mathbf{n}}. \quad (7)$$

By the Central Limit Theorem, for large \mathbf{n} , the sample mean $\bar{\Lambda}$ approximates a Gaussian distribution $\bar{\Lambda} \sim \mathcal{N}\left(f(\boldsymbol{\theta}), \frac{\sigma^2(\boldsymbol{\theta})}{\mathbf{n}}\right)$. Thus, each evaluation of $f(\boldsymbol{\theta})$ is subject to zero-mean Gaussian noise:

$$\tilde{f}(\boldsymbol{\theta}) = f(\boldsymbol{\theta}) + \mathcal{N}\left(0, \frac{\sigma^2(\boldsymbol{\theta})}{\mathbf{n}}\right). \quad (8)$$

This noise arises from statistical nature of quantum measurements. In real quantum systems, there are also various hardware-induced noise sources (e.g., decoherence, gate errors). For unbiased noises, according to the Central Limit Theorem again, their effect in the sample mean can also be approximated as Gaussian, and thus can be incorporated into the same mathematical framework.

2.2 Setting II: trigonometric representation from quantum circuit structures

Another feature of the cost function $f(\boldsymbol{\theta})$ is that it can be expressed as a trigonometric polynomial, which is the key for designing our OICD method. Consider a parameter vector $\boldsymbol{\theta} \in \mathbb{R}^m$, where all entries are fixed except for $\theta_j \in \mathbb{R}$ ($j = 1, \dots, m$). When we optimize a single variable θ_j , the operations unrelated to θ_j can be absorbed into the input state and the observable. This leads to the following univariate cost function,

$$\theta_j \mapsto f(\theta_j) = \langle \psi | U_j(\theta_j)^\dagger M' U_j(\theta_j) | \psi \rangle, \quad (9)$$

where $|\psi\rangle := V_{j-1} U_{j-1}(\theta_{j-1}) \cdots V_1 U_1(\theta_1) |0\rangle$ is the state prepared by the subcircuit preceding $U_j(\theta_j)$, and $M' := V_j^\dagger \cdots U_m(\theta_m)^\dagger V_m^\dagger M V_m U_m(\theta_m) \cdots V_j$ includes the subcircuit following $U_j(\theta_j)$. Throughout the paper, we refer to $\theta_j \mapsto f(\theta_j)$ as the *restricted univariate function* of $f(\boldsymbol{\theta})$. For notation convenience, we simply write it as $f(\theta_j)$, and we can distinguish it from the original multivariate function by the argument, whether θ_j or $\boldsymbol{\theta}$.

For a fixed index $j = 1, \dots, m$, let the eigenvalues of H_j in Eq. (3) be denoted by $\{\lambda_l^j\}_{l=1}^N$, and define the set of all unique positive differences between these eigenvalues, referred to as the *frequencies*, to be

$$\{\Omega_k^j\}_{k=1}^{r_j} := \{|\lambda_l^j - \lambda_{l'}^j| > 0 \mid \forall l, l' = 1, \dots, N\}, \quad (10)$$

where $r_j := |\{\Omega_k^j\}|$. Here, the frequencies $\{\Omega_k^j\}_{k=1}^{r_j}$ is re-indexed in ascending order. According to [20], the restricted univariate function in Eq. (9) can be expressed as a trigonometric polynomial (a finite-term Fourier series) as

$$f(\theta_j) = \frac{1}{\sqrt{2}} a_0 + \sum_{k=1}^{r_j} \left[a_k \cos(\Omega_k^j \theta_j) + b_k \sin(\Omega_k^j \theta_j) \right], \quad (11)$$

where a_0, a_k and b_k are some real coefficients. This representation of $f(\theta_j)$ as a trigonometric polynomial succinctly captures the dependence of the cost function on the single parameter θ_j , with each term oscillating at distinct frequencies determined by the eigenvalue differences of the generator H_j .

For completeness, we provide a detailed proof of Eq. (11) in Appendix A. It should be noted that whenever we consider $f(\theta_j)$, we implicitly fix the values of the other $m - 1$ parameters θ_i 's. As these fixed parameters change, the univariate function $f(\theta_j)$ also changes. This is reflected in the varying coefficients a_0, a_k , and b_k in Eq. (11), while $\{\Omega_k^j\}_{k=1}^{r_j}$ remains unchanged. The trigonometric nature of the cost function arises primarily from the specific circuit structure in Eq. (2), especially since the parameterized gates are defined using rotation-like gates $e^{iH_j\theta_j}$.

2.3 Reformulated problem

We are now ready to reformulate Eq. (1) from the perspective of optimization theory.

Problem 1 (Reformulated PQC Optimization Problem). *The goal is to find an efficient algorithm to solve the optimization problem,*

$$\boldsymbol{\theta}^* = \operatorname{argmin}_{\boldsymbol{\theta} \in \mathbb{R}^m} f(\boldsymbol{\theta}), \quad (12)$$

under the following settings.

Setting I *Each function evaluation of $f(\boldsymbol{\theta})$ is subject to zero-mean Gaussian noise. Specifically, this gives rise to a random variable $\tilde{f}(\boldsymbol{\theta})$ defined as*

$$\tilde{f}(\boldsymbol{\theta}) = f(\boldsymbol{\theta}) + \mathcal{N}\left(0, \frac{\sigma^2(\boldsymbol{\theta})}{\mathbf{n}}\right). \quad (13)$$

Setting II *For each coordinate $j = 1, \dots, m$, the restricted univariate function Eq. (9) of $f(\boldsymbol{\theta})$, has the trigonometric polynomial form*

$$f(\theta_j) = \frac{1}{\sqrt{2}} a_0 + \sum_{k=1}^{r_j} \left[a_k \cos(\Omega_k^j \theta_j) + b_k \sin(\Omega_k^j \theta_j) \right], \quad (14)$$

where a_0, a_k and b_k are real coefficients determined by the remaining θ_i 's with $i \neq j$.

We will make further assumptions on the variance. While the variance of an individual measurement, $\sigma^2(\boldsymbol{\theta})$, technically depends on $\boldsymbol{\theta}$ as in Eq. (7), evaluating the variance is often computationally prohibitive. Following the convention in existing studies [21, 20, 26], we consider the following assumption, which is usually a good approximation in practice.

Assumption 1 (Constant variance). *We assume a constant noise level as follows: given any $\boldsymbol{\theta}$, $\sigma^2(\boldsymbol{\theta}) \approx \sigma^2(\boldsymbol{\theta} + s\mathbf{e}_j)$ for all $s \in \mathbb{R}$. Here, \mathbf{e}_j represents the standard basis vector in the j -th direction.*

3 Optimal interpolation-based coordinate descent (OICD) method

In this section, we will propose our optimal interpolation-based coordinate descent (OICD) method for solving Problem 1.

3.1 Overview

We first provide an overview of the original coordinate descent (CD) method [27]. The original CD method to Problem 1 works as follows: given current parameters $\boldsymbol{\theta}$, we first select a coordinate j and consider the restricted univariate function $f(\theta_j)$ as in Eq. (14). Then, we update the j -th component of $\boldsymbol{\theta}$ by

$$\theta_j^{new} \leftarrow \underset{\theta_j \in \mathbb{R}}{\operatorname{argmin}} f(\theta_j), \quad (15)$$

which is simply a single-variable optimization subproblem and is easy to solve. Usually, one uses the gradient descent method to solve the subproblem Eq. (15). When the index j is selected randomly, and a single step is taken in the direction of the negative gradient (which, in our case, becomes a negative derivative) with some learning rate $\alpha > 0$ as

$$\theta_j^{new} \leftarrow \theta_j^{old} - \alpha \left. \frac{df(\theta_j)}{d\theta_j} \right|_{\theta_j = \theta_j^{old}}, \quad (16)$$

the CD method becomes the famous random coordinate descent (RCD) [22]. After updating coordinate j , we next select a new coordinate and repeat the above process.

No matter what method we use to solve the subproblem in Eq. (15), the CD method updates only one parameter at each iteration. However, it can be computationally expensive to directly apply existing solvers to Eq. (15), because most solvers rely on iterative methods requiring numerous function evaluations $\theta_j \mapsto f(\theta_j)$. In VQAs context, each function evaluation necessitates re-tuning the quantum device parameters and repeating measurements, making this approach prohibitively expensive in terms of both time and quantum resources.

To address this issue, we leverage the trigonometric structure of the cost function in Setting II. Our approach is to recover the coefficients a_0 , a_k , and b_k in Eq. (14) using the *interpolation method* (which will be discussed in the next subsection). This method involves only a limited number (specifically $2r_j + 1$) of evaluations of $f(\theta_j)$ at different points. On the other hand, since function evaluations are always noisy as per Setting I, the recovered function can never be exact: it will only serve as an approximation to Eq. (14). Then, with the approximated function

$$\theta_j \mapsto \hat{f}(\theta_j) = \frac{1}{\sqrt{2}} \hat{a}_0 + \sum_{k=1}^{r_j} [\hat{a}_k \cos(\Omega_k^j \theta_j) + \hat{b}_k \sin(\Omega_k^j \theta_j)] \quad (17)$$

in hand (symbol $\hat{\cdot}$ indicates an estimated value for true value), we will solve an approximated subproblem

$$\theta_j^{new} \leftarrow \underset{\theta_j \in \mathbb{R}}{\operatorname{argmin}} \hat{f}(\theta_j). \quad (18)$$

Importantly, all the information of \hat{f} (i.e., the estimated $\hat{a}_0, \hat{a}_k, \hat{b}_k$) is stored on the classical computer, and the callings of $\theta_j \mapsto \hat{f}(\theta_j)$ are completely independent of the quantum device. As a result, there is no additional quantum-related burden in solving Eq. (18). The other process remains the same as in the original CD. We call this the interpolation-based coordinate descent (ICD) method to Problem 1.

In the simplest case where $r_j = 1$ and $\Omega_k^j = 1$, we will solve

$$\theta_j^{new} \leftarrow \underset{\theta_j \in \mathbb{R}}{\operatorname{argmin}} \hat{f}(\theta_j) = \frac{1}{\sqrt{2}} \hat{a}_0 + \hat{a}_1 \cos(\theta_j) + \hat{b}_1 \sin(\theta_j), \quad (19)$$

which has a closed-form solution $\theta_j^{new} \leftarrow \theta_j^* = \arctan\left(\frac{\hat{b}_1}{\hat{a}_1}\right)$. This special case has been studied in [28]. In the general case $r_j \geq 2$, there is no closed-form solution any more, however, we can adopt an eigenvalue method (discussed in Appendix F) to exactly solve the approximated subproblem in Eq. (18).

Clearly, the effectiveness of the ICD method lies in how to best recover the approximation function $\hat{f}(\theta_j)$ for true function $f(\theta_j)$ in the presence of unavoidable noise. The accuracy of the solution to the approximated subproblem Eq. (18), relative to the exact subproblem Eq. (15), is directly determined by the error between \hat{f} and f . In subsequent subsections, we will demonstrate how to enhance the interpolation method to minimize noise impact.

3.2 Interpolation method to recover restricted univariate functions

In this subsection, we discuss how to perform interpolation to recover the restricted univariate function in Eq. (14). For notation simplicity, we omit index j and replace the variable θ_j with x , and consider the trigonometric polynomial $f: \mathbb{R} \rightarrow \mathbb{R}$ of order r

$$f(x) = \frac{1}{\sqrt{2}} a_0 + \sum_{k=1}^r [a_k \cos(\Omega_k x) + b_k \sin(\Omega_k x)], \quad (20)$$

where a_k 's and b_k 's are $n \equiv 2r+1$ many unknown real parameters. Due to the specific construction, all information about f is equivalent to these coefficients. The goal of the interpolation is to recover all coefficients above by evaluating the function $f(x)$ at various points x . We next discuss the noise-free case and the noisy case, respectively.

3.2.1 Interpolation with true data

Suppose we have access to the calling $x \mapsto f(x)$ without noise for any argument x . This case is the foundation for our subsequent consideration of interpolation under noise. Indeed, knowing any set of n distinct true data points $\{(x_i, f(x_i))\}_{i=0}^{2r}$ allows us to *exactly* recover the coefficient vector

$$\mathbf{z} := [a_0, a_1, b_1, \dots, a_r, b_r]^\dagger \in \mathbb{R}^n, \quad (21)$$

thereby giving us a complete understanding of f in Eq. (20). Let $\mathbf{x} := [x_0, x_1, \dots, x_{2r}]^\dagger \in \mathbb{R}^n$ with distinct entries. Define the *true data vector*

$$\mathbf{y}_{\mathbf{x}} := [f(x_0), f(x_1), \dots, f(x_{2r})]^\dagger \in \mathbb{R}^n. \quad (22)$$

Now, using the chosen \mathbf{x} , we construct the interpolation matrix

$$A_{\mathbf{x}} := \begin{bmatrix} \frac{1}{\sqrt{2}} & \cos(\Omega_1 x_0) & \sin(\Omega_1 x_0) & \cdots & \cos(\Omega_r x_0) & \sin(\Omega_r x_0) \\ \frac{1}{\sqrt{2}} & \cos(\Omega_1 x_1) & \sin(\Omega_1 x_1) & \cdots & \cos(\Omega_r x_1) & \sin(\Omega_r x_1) \\ \vdots & \vdots & \vdots & \ddots & \vdots & \vdots \\ \frac{1}{\sqrt{2}} & \cos(\Omega_1 x_{2r}) & \sin(\Omega_1 x_{2r}) & \cdots & \cos(\Omega_r x_{2r}) & \sin(\Omega_r x_{2r}) \end{bmatrix} \in \mathbb{R}^{n \times n}. \quad (23)$$

Given these definitions, we can solve the linear equation

$$A_{\mathbf{x}} \mathbf{z} = \mathbf{y}_{\mathbf{x}} \quad (24)$$

to recover the coefficient \mathbf{z} . Here, \mathbf{x} serves as a set of *interpolation nodes*. Moreover, due to the special structure of $\mathbf{y}_{\mathbf{x}}$ and $A_{\mathbf{x}}$ in Eq. (22) and Eq. (23), the solution $\mathbf{z} \equiv A_{\mathbf{x}}^{-1} \mathbf{y}_{\mathbf{x}}$ is independent of \mathbf{x} . This implies that any interpolation nodes \mathbf{x} yield exactly the same results. It should be noted that this property holds only in the ideal setting where we can evaluate $x \mapsto f(x)$ without noise.

Actually, here, we implicitly assume that the chosen \mathbf{x} results in a non-singular $A_{\mathbf{x}}$. Since $A_{\mathbf{x}}$ contains parameters Ω_k , it is difficult to derive the condition for \mathbf{x} that guarantees non-singularity. In the practical algorithm later, we will use an optimally chosen \mathbf{x}^* by solving Eq. (34), which naturally ensures that $A_{\mathbf{x}^*}$ is non-singular. In Section 4, for the case of $\Omega_k = k$ for any k , we can prove that the condition for $A_{\mathbf{x}}$ to be non-singular is precisely that all entries of \mathbf{x} are distinct modulo 2π .

3.2.2 Interpolation with noisy data

In practice, we can only access the function $x \mapsto f(x)$ with noise. According to Setting I and Eq. (13), the observed value of $f(x)$ has an additive zero-mean Gaussian noise $\epsilon_x \sim \mathcal{N}(0, \frac{\sigma^2(x)}{\mathbf{n}})$. By Assumption 1, the variance $\sigma^2(x)$ is independent of x , allowing us to simply denote it as σ^2 . Since we always consider a constant number \mathbf{n} throughout this paper, \mathbf{n} can be absorbed into σ^2 . Then we simply have $\epsilon_x \sim \mathcal{N}(0, \sigma^2)$, and each evaluation of the cost function gives noisy data as a random variable

$$\tilde{f}(x) = f(x) + \epsilon_x, \quad \epsilon_x \sim \mathcal{N}(0, \sigma^2). \quad (25)$$

Now, given n many noisy data points $\{(x_i, \tilde{f}(x_i))\}_{i=0}^{2r}$, rather than solving Eq. (24), we will address its perturbed version:

$$A_{\mathbf{x}} \hat{\mathbf{z}}_{\mathbf{x}} = \mathbf{y}_{\text{obs}} := \mathbf{y}_{\mathbf{x}} + \mathbf{e}, \quad (26)$$

where $\mathbf{e} = [\epsilon_0, \epsilon_1, \dots, \epsilon_{2r}]^\dagger \sim \mathcal{N}(0, \sigma^2 I)$ is the normal random vector, $\mathbf{y}_{\mathbf{x}}$ is still the true (but unknown) data vector as Eq. (22), and

$$\hat{\mathbf{z}}_{\mathbf{x}} = [\hat{a}_0, \hat{a}_1, \hat{b}_1, \dots, \hat{a}_r, \hat{b}_r]^\dagger \in \mathbb{R}^n \quad (27)$$

is solution of the perturbed equation. In fact, $\hat{\mathbf{z}}_{\mathbf{x}}$ is an estimator of the exact coefficients \mathbf{z} . We have

$$\hat{\mathbf{z}}_{\mathbf{x}} = A_{\mathbf{x}}^{-1}(\mathbf{y}_{\mathbf{x}} + \mathbf{e}) = \mathbf{z} + A_{\mathbf{x}}^{-1}\mathbf{e}. \quad (28)$$

Notice that \mathbf{e} is normal, and $\hat{\mathbf{z}}_{\mathbf{x}} = \mathbf{z} + A_{\mathbf{x}}^{-1}\mathbf{e}$ represents an affine transformation of \mathbf{e} , so $\hat{\mathbf{z}}_{\mathbf{x}}$ is also a normal random vector. Moreover, we have

$$\mathbb{E}[\hat{\mathbf{z}}_{\mathbf{x}}] = \mathbf{z} + A_{\mathbf{x}}^{-1} \mathbb{E}[\mathbf{e}] = \mathbf{z}, \quad (29)$$

and the covariance matrix of $\hat{\mathbf{z}}_{\mathbf{x}}$ is

$$\text{VAR}[\hat{\mathbf{z}}_{\mathbf{x}}] = \mathbb{E}[(\hat{\mathbf{z}}_{\mathbf{x}} - \mathbf{z})(\hat{\mathbf{z}}_{\mathbf{x}} - \mathbf{z})^\dagger] = A_{\mathbf{x}}^{-1} \mathbb{E}[\mathbf{e}\mathbf{e}^\dagger] (A_{\mathbf{x}}^{-1})^\dagger = \sigma^2 [A_{\mathbf{x}}^\dagger A_{\mathbf{x}}]^{-1}. \quad (30)$$

It is evident that $\hat{\mathbf{z}}_{\mathbf{x}}$ serves as an unbiased estimator of the true coefficients \mathbf{z} . However, its variance depends on the interpolation nodes \mathbf{x} . This naturally raises the question: can we determine optimal interpolation nodes \mathbf{x} that provide the best possible approximation to the true coefficients \mathbf{z} ?

To quantify the estimation error of $\hat{\mathbf{z}}_{\mathbf{x}}$ with respect to the true \mathbf{z} , a common metric is the mean squared error (MSE). Let the estimation error be defined as

$$\Delta \mathbf{z}_{\mathbf{x}} := \hat{\mathbf{z}}_{\mathbf{x}} - \mathbf{z} = A_{\mathbf{x}}^{-1} \mathbf{e}. \quad (31)$$

The MSE of $\hat{\mathbf{z}}$ is then given by $\text{MSE}(\hat{\mathbf{z}}_{\mathbf{x}}) := \mathbb{E}[\|\hat{\mathbf{z}}_{\mathbf{x}} - \mathbb{E}[\hat{\mathbf{z}}_{\mathbf{x}}]\|^2] = \mathbb{E}[\|\Delta \mathbf{z}_{\mathbf{x}}\|^2]$. Indeed, we have

$$\text{MSE}(\hat{\mathbf{z}}_{\mathbf{x}}) = \mathbb{E}[\text{tr}((A_{\mathbf{x}}^{-1}\mathbf{e})^\dagger (A_{\mathbf{x}}^{-1}\mathbf{e}))] = \mathbb{E}[\text{tr}((A_{\mathbf{x}}^{-1}\mathbf{e})(A_{\mathbf{x}}^{-1}\mathbf{e})^\dagger)] \quad (32)$$

$$= \text{tr}(\mathbb{E}[(A_{\mathbf{x}}^{-1}\mathbf{e})(A_{\mathbf{x}}^{-1}\mathbf{e})^\dagger]) = \sigma^2 \text{tr}([A_{\mathbf{x}}^\dagger A_{\mathbf{x}}]^{-1}) = \sigma^2 \|A_{\mathbf{x}}^{-1}\|_F^2, \quad (33)$$

where $\|\cdot\|_F$ is the Frobenius norm, i.e., $\|X\|_F = \sqrt{\text{tr}(X^\dagger X)}$. The second-to-last equality follows from Eq. (30).

Clearly, the mean squared error $\text{MSE}(\hat{\mathbf{z}}_{\mathbf{x}})$ depends on the specific choice of interpolation nodes \mathbf{x} . Naturally, we seek to select the optimal

$$\mathbf{x}^* = \underset{\mathbf{x} \in \mathbb{R}^n}{\text{argmin}} \text{MSE}(\hat{\mathbf{z}}_{\mathbf{x}}) = \sigma^2 \|A_{\mathbf{x}^*}^{-1}\|_F^2, \quad (34)$$

to achieve the best approximation, which is equivalent to minimizing $\|A_{\mathbf{x}}^{-1}\|_F^2$ since σ^2 is a constant. We observe that minimizing $\|A_{\mathbf{x}}^{-1}\|_F^2$ inherently forces $A_{\mathbf{x}}$ to be invertible; otherwise, the objective value would tend to infinity. Since $A_{\mathbf{x}}$ in Eq. (23) involves complicated parameters Ω_k , it is difficult to obtain an analytical solution \mathbf{x}^* to Eq. (34). However, a numerical solution is sufficient for our algorithmic design. In practice, we can use common algorithms like Adam to solve it. In Section 4, we will show that for the equidistant frequency case ($\forall \Omega_k = k$), a global optimal analytical solution to Eq. (34) exists.

3.3 Vanilla OICD algorithm

Building on the previous subsections, we now formally introduce the optimal interpolation-based coordinate descent (OICD) method for solving Problem 1. First, we introduce the vanilla OICD in Algorithm 1. As discussed in Section 3.1, a key initial step of OICD is to obtain the optimal interpolation nodes $\mathbf{x}^{j,*}$ and corresponding interpolation matrices $A_{\mathbf{x}^{j,*}}$ for each $j = 1, \dots, m$. To clarify this step, we present it separately in Algorithm 2. Note that this is a preparatory step, and the interpolation schemes generated here can be reused in each iteration of OICD Algorithm 1.

Algorithm 1: Vanilla OICD Method for Problem 1

Input : Initial parameters $\boldsymbol{\theta}^0 = [\theta_1^0, \dots, \theta_m^0]^\dagger$, and the number of iterations \mathbb{T} .

Output: Optimized parameters $\boldsymbol{\theta}^\mathbb{T}$ after \mathbb{T} iterations.

- 1 Obtain the optimal interpolation schemes $\{(\mathbf{x}^{j,*}, A_{\mathbf{x}^{j,*}}^{-1})\}_{j=1}^m$ using Algorithm 2;
 - 2 **for** $t = 0$ **to** \mathbb{T} **do**
 - 3 Select a coordinate $j \in \{1, \dots, m\}$, either sequentially or uniformly at random;
 - 4 Fix all parameters of $\boldsymbol{\theta}^t$ except for θ_j^t , and consider the restricted univariate function $\theta_j \mapsto f(\theta_j)$ in Eq. (17);
 - 5 This is the only quantum burden required to construct the observed data vector at $\mathbf{x}^{j,*}$, i.e.,

$$\mathbf{y}_{\text{obs}} := [\tilde{f}(x_0^{j,*}), \tilde{f}(x_1^{j,*}), \dots, \tilde{f}(x_{2r_j}^{j,*})]^\dagger; \quad (35)$$
 - Compute the estimated coefficients $\hat{\mathbf{z}} := A_{\mathbf{x}^{j,*}}^{-1} \mathbf{y}_{\text{obs}}$ and recover the estimated function $\hat{f}(\theta_j)$ as in Eq. (17);
 - 6 Let $\theta_j^{t+1} := \underset{\theta_j \in \mathbb{R}}{\operatorname{argmin}} \hat{f}(\theta_j)$;
 - 7 Let $\theta_i^{t+1} := \theta_i^t$ for all $i \neq j$;
 - 8 **end**
-

Algorithm 2: Obtain the Optimal Interpolation Schemes for General Frequencies

Input : All Hermitian generators $H_j \in \mathbb{C}^{N \times N}$, $j = 1, \dots, m$, in Eq. (3).

Output: Optimal interpolation nodes $\mathbf{x}^{j,*}$ and inverse of optimal interpolation matrices $A_{\mathbf{x}^{j,*}}^{-1}$, $j = 1, \dots, m$.

- 1 **for** $j = 1, \dots, m$ **do**
 - 2 Determine the frequency set $\{\Omega_k^j\}_{k=1}^{r_j}$ of H_j as defined in Eq. (10);
 - 3 Let $n_j := 2r_j + 1$. Consider the associated interpolation matrix $A_{\mathbf{x}} \in \mathbb{R}^{n_j \times n_j}$ defined in Eq. (23) based on the computed frequencies;
 - 4 Solve for the optimal interpolation nodes $\mathbf{x}^{j,*} := \underset{\mathbf{x} \in \mathbb{R}^{n_j}}{\operatorname{argmin}} \|A_{\mathbf{x}}^{-1}\|_F^2$;
 - 5 Compute the inverse^a of optimal interpolation matrix $A_{\mathbf{x}^{j,*}}^{-1}$;
 - 6 **end**
-

^aWe explicitly compute the inverse of $A_{\mathbf{x}^{j,*}}$ for two reasons: 1. In practice, the scale of $A_{\mathbf{x}^{j,*}}$ is small. 2. During the iterations, we need to repeatedly solve the equation $A_{\mathbf{x}^{j,*}} \hat{\mathbf{z}} = \mathbf{y}_{\text{obs}}$. Note that $A_{\mathbf{x}^{j,*}}$ is fixed, while \mathbf{y}_{obs} is constantly updated. Therefore, computing the inverse of $A_{\mathbf{x}^{j,*}}$ once and solving the equation using $\hat{\mathbf{z}} = A_{\mathbf{x}^{j,*}}^{-1} \mathbf{y}_{\text{obs}}$ is more efficient.

3.4 Practical OICD algorithm

In the vanilla OICD Algorithm 1, each interpolation requires $2r_j + 1$ function evaluations. In the following, we propose a practical OICD Algorithm 3, which is essentially the same as the vanilla OICD but only requires $2r_j$ function evaluations per iteration (the same as in RCD). Algorithm 3 is the implementation version of our code. The differences from Algorithm 1 are marked with \blacktriangleright .

Algorithm 3: Practical OICD Method for Problem 1

Input : Initial parameters $\boldsymbol{\theta}^0 = [\theta_1^0, \dots, \theta_m^0]^\dagger$, and the number of iterations T .
Output: Optimized parameters $\boldsymbol{\theta}^\mathsf{T}$ after T iterations.

- 1 Obtain the optimal interpolation schemes $\{(\mathbf{x}^{j,*}, A_{\mathbf{x}^{j,*}}^{-1})\}_{j=1}^m$ using Algorithm 2;
- 2 \blacktriangleright Compute initial function value $\hat{f}^0 := \tilde{f}(\boldsymbol{\theta}^0)$;
- 3 **for** $t = 0$ **to** T **do**
- 4 Select a coordinate $j \in \{1, \dots, m\}$, either sequentially or uniformly at random;
- 5 Fix all parameters of $\boldsymbol{\theta}^t$ except for θ_j^t , and consider the restricted univariate function $\theta_j \mapsto f(\theta_j)$ in Eq. (17);
- 6 \blacktriangleright (quantum burden) Construct the observed data vector at $\mathbf{x}^{j,*}$ but starting from θ_j^t , i.e.,

$$\mathbf{y}_{\text{obs}} := [\tilde{f}(\theta_j^t), \tilde{f}(\theta_j^t + (x_1^{j,*} - x_0^{j,*})), \dots, \tilde{f}(\theta_j^t + (x_{2r}^{j,*} - x_0^{j,*}))]^\dagger, \quad (36)$$
 and $\tilde{f}(\theta_j^t)$ is replaced by \hat{f}^t ;
- 7 \blacktriangleright Construct the matrix E_s^{-1} in Eq. (101) with $s := \theta_j^t - x_0^{j,*}$;
- 8 \blacktriangleright Compute the estimated coefficients $\hat{\mathbf{z}} := E_s^{-1} A_{\mathbf{x}^{j,*}}^{-1} \mathbf{y}_{\text{obs}}$ and recover the estimated function $\hat{f}(\theta_j)$ as in Eq. (17);
- 9 Let $\theta_j^{t+1} := \underset{\theta_j \in \mathbb{R}}{\text{argmin}} \hat{f}(\theta_j)$;
- 10 Let $\theta_i^{t+1} := \theta_i^t$ for all $i \neq j$;
- 11 \blacktriangleright Record $\hat{f}^{t+1} := \hat{f}(\theta_j^{t+1})$;
- 12 **end**

Building on the two observations discussed in Appendix C, we now briefly explain the rationale behind Algorithm 1. Due to the shift invariance of interpolations, as shown in Lemma 1 in Appendix C.1, we can freely choose the first interpolation node without affecting the optimality of Eq. (34). In the t -th iteration of Algorithm 3, after selecting coordinate j , we deliberately set the first node to be the current value at j , i.e., θ_j^t . This choice is motivated by the following reasoning.

Consider the previous iteration $\boldsymbol{\theta}^{t-1} = [\theta_1^{t-1}, \dots, \theta_k^{t-1}, \dots, \theta_m^{t-1}]^\dagger$. After selecting coordinate k , we update $\theta_k^{t-1} \rightarrow \theta_k^t := \underset{\theta_k}{\text{argmin}} \hat{f}(\theta_k)$, and the new point becomes $\boldsymbol{\theta}^t = [\theta_1^{t-1}, \dots, \theta_k^t, \dots, \theta_m^{t-1}]^\dagger$. From the unbiasedness of the approximated function, as shown in Appendix C.2, we know that

$$\mathbb{E}[\hat{f}(\theta_k^t)] = f(\boldsymbol{\theta}^t). \quad (37)$$

In the t -th iteration, we select another coordinate j . Due to the properties of \tilde{f} , we also have

$$\mathbb{E}[\tilde{f}(\theta_j^t)] = f(\boldsymbol{\theta}^t). \quad (38)$$

Thus, both $\hat{f}(\theta_k^t)$ and $\tilde{f}(\theta_j^t)$ are unbiased estimates of $f(\boldsymbol{\theta}^t)$. This means that $\hat{f}(\theta_k^t)$ can replace $\tilde{f}(\theta_j^t)$, allowing us to reduce one function evaluation when we set the first interpolation node to θ_j^t . Additionally, by using Lemma 1, the inverse of the shifted interpolation matrix can be computed efficiently, i.e., $E_s^{-1} A_{\mathbf{x}^{j,*}}^{-1}$. Combining these considerations, we describe the practical OICD algorithm in Algorithm 3.

4 Optimal interpolation nodes for equidistant frequencies

So far, all the discussions have been for the general frequency Ω_k , which appears in Eq. (14) of Setting II. This section discusses the equidistant frequency case, which is the most common in practical applications. Moreover, in this case, our proposed OICD algorithm has many elegant

theoretical results. More specifically, throughout this section, we adopt the following assumption [20].

Assumption 2 (Equidistant frequencies). *For every H_j in Eq. (2), we assume the frequencies $\{\Omega_k^j\}_{k=1}^{r_j}$ are equidistant, i.e., $\Omega_k^j = k\Omega^j$ ($k = 1, \dots, r_j$) for some constant Ω^j . Without loss of generality², we further restrict the frequencies to integer values, i.e., $\Omega_k^j = k$ ($k = 1, \dots, r_j$).*

The equidistant frequency patterns often arise in practical scenarios. A particularly important case occurs when the Hermitian operator H_j can be expressed as a sum of R commuting Pauli words \mathcal{P}_k with coefficients of ± 1 , i.e., $H_j = \sum_{k=1}^R \pm \mathcal{P}_k$. This structure results in equidistant frequencies and $r_j = R$. Notice that while equidistant eigenvalues do imply equidistant frequencies, the converse is not always true. It is possible for a Hermitian operator to have non-equidistant eigenvalues but still produce equidistant frequencies, e.g., H_j has three distinct $\lambda_1 = 0, \lambda_2 = 1, \lambda_3 = 3$.

For the equidistant frequencies case, the previously proposed Algorithm 3 can be directly applied without any modification. Moreover, the corresponding optimal interpolation nodes \mathbf{x}^* have analytical solutions, allowing us to skip the entire process of Algorithm 2.

4.1 Optimal interpolation nodes are $\frac{2\pi}{n}$ -equidistant nodes

We again use the notations in Section 3.2 without the index j . As shown in Appendix B, if the interpolation nodes $\mathbf{x} = [x_0, x_1, \dots, x_{2r}]^\dagger \in \mathbb{R}^n$ have distinct entries modulo 2π , the matrix $A_{\mathbf{x}}$ must be non-singular, ensuring that $\hat{\mathbf{z}}_{\mathbf{x}}$ in Eq. (26) is well-defined.

The main findings of this subsection can be summarized as follows: the $\frac{2\pi}{n}$ -equidistant nodes $\mathbf{x}^* \in \mathbb{R}^n$ with $n = 2r + 1$, defined by

$$x_k^* = s + \frac{2\pi}{n}k, \quad k = 0, 1, \dots, 2r, \quad (39)$$

where $s \in \mathbb{R}$ is a shift value, achieve global optimality under the following three criteria simultaneously (and independently of s):

1. Minimization of the mean squared error, $\text{MSE}(\hat{\mathbf{z}}_{\mathbf{x}})$.
2. Minimization of the condition number of the interpolation matrix $A_{\mathbf{x}}$.
3. Minimization of the average variance of the estimated derivatives $\hat{f}^{(d)}(x)$ of all orders $d \geq 0$.

In the following, we examine each of these optimality criteria in detail.

4.1.1 Criteria I: minimal mean squared error

The following theorem helps us directly obtain the results of Algorithm 2 for the case of equidistant frequencies. For proofs, see Appendix D.3.

Theorem 1 (Minimal Mean Squared Error). *When Assumption 2 holds, the $\frac{2\pi}{n}$ -equidistant nodes \mathbf{x}^* with an arbitrary shift value, as defined in Eq. (39), globally solves*

$$\mathbf{x}^* = \underset{\substack{\mathbf{x} \in \mathbb{R}^n \\ x_i \text{ distinct modulo } 2\pi}}{\operatorname{argmin}} \quad \text{MSE}(\hat{\mathbf{z}}_{\mathbf{x}}) = \sigma^2 \|A_{\mathbf{x}}^{-1}\|_F^2, \quad (40)$$

where the global minimum is $2\sigma^2$.

²For $\Omega^j \neq 1$, we can rescale the function argument to achieve $\Omega_k^j = k$. Once the rescaled function is constructed, the original function is readily available.

4.1.2 Criteria II: minimal condition number

We can also analyze the stability of linear equation from the perspective of classical numerical analysis. Using estimation error $\Delta \mathbf{z}_\mathbf{x} = \hat{\mathbf{z}}_\mathbf{x} - \mathbf{z}$, we can rewrite the perturbed linear equation Eq. (26) as

$$A_\mathbf{x}(\Delta \mathbf{z}_\mathbf{x} + \mathbf{z}) = \mathbf{y}_\mathbf{x} + \mathbf{e}. \quad (41)$$

Let $\|\cdot\|_2$ stand for the spectral norm and the condition number $\kappa_2(A_\mathbf{x}) = \|A_\mathbf{x}\|_2 \|A_\mathbf{x}^{-1}\|_2$. Based on standard results in numerical stability analysis [29], $\kappa_2(A_\mathbf{x})$ provides an upper bound on the relative error by inequality

$$\frac{\|\Delta \mathbf{z}_\mathbf{x}\|}{\|\mathbf{z}\|} \leq \kappa_2(A_\mathbf{x}) \frac{\|\mathbf{e}\|}{\|\mathbf{y}_\mathbf{x}\|}. \quad (42)$$

This reveals that a smaller condition number of interpolation matrix $A_\mathbf{x}$ ensures better numerical stability for solutions. This motivates us to seek interpolation nodes that minimize $\kappa_2(A_\mathbf{x})$, leading to the following theorem. For proofs, see Appendix D.4.

Theorem 2 (Minimal Condition Number). *When Assumption 2 holds, the $\frac{2\pi}{n}$ -equidistant nodes \mathbf{x}^* with an arbitrary shift value, as defined in Eq. (39), globally solves*

$$\mathbf{x}^* = \underset{\substack{\mathbf{x} \in \mathbb{R}^n \\ x_i \text{ distinct modulo } 2\pi}}{\operatorname{argmin}} \kappa_2(A_\mathbf{x}), \quad (43)$$

where the global minimum is 1.

Since the condition number of any matrix is always greater than or equal to 1, we have achieved the minimal condition number, even in our cases where $A_\mathbf{x}$ possesses specific structural characteristics as in Eq. (23).

4.1.3 Criteria III: minimal average variance of derivatives

In Appendix C.2, we have discussed the variance $\operatorname{Var}[\hat{f}(x)]$, which quantifies the approximation accuracy of \hat{f} to the true function f . If we treat $\hat{f}^{(0)} \equiv \hat{f}$ and $f^{(0)} \equiv f$ as zero-order derivatives, a similar discussion can be extended to derivatives of any d order. Let $\mathbf{t}^{(0)}(x) \equiv \mathbf{t}(x)$ defined as

$$\mathbf{t}(x) := [1/\sqrt{2}, \cos(\Omega_1 x), \sin(\Omega_1 x), \dots, \cos(\Omega_r x), \sin(\Omega_r x)]^\dagger \in \mathbb{R}^n, \quad (44)$$

and for any integer $d \geq 1$, let

$$\mathbf{t}^{(d)}(x) := \begin{bmatrix} 0 \\ \Omega_1^d \cos(\Omega_1 x + \frac{d\pi}{2}) \\ \Omega_1^d \sin(\Omega_1 x + \frac{d\pi}{2}) \\ \vdots \\ \Omega_r^d \cos(\Omega_r x + \frac{d\pi}{2}) \\ \Omega_r^d \sin(\Omega_r x + \frac{d\pi}{2}) \end{bmatrix} \in \mathbb{R}^n \quad (45)$$

denote the d -th derivative of $\mathbf{t}^{(0)}(x)$. Then, the d -th order derivative of $\hat{f}(x)$ is $\hat{f}^{(d)}(x) = \mathbf{t}^{(d)}(x)^\dagger \hat{\mathbf{z}}_\mathbf{x}$. Similar to the discussion in Appendix C.2, $\hat{f}^{(d)}(x)$ is normal and unbiased estimates of the true derivatives $f^{(d)}(x)$ since

$$\mathbb{E}[\hat{f}^{(d)}(x)] = f^{(d)}(x). \quad (46)$$

Again by Lemma 11 of Appendix D.5,

$$\operatorname{Var}[\hat{f}^{(d)}(x)] = \langle \operatorname{VAR}[\hat{\mathbf{z}}_\mathbf{x}], \mathbf{t}^{(d)}(x) \mathbf{t}^{(d)}(x)^\dagger \rangle. \quad (47)$$

Rather than focusing on the variance at specific x , we are more interested in the average variance of $\hat{f}^{(d)}(x)$ over its domain. When Assumption 2 holds ($\forall \Omega_k = k$), both $f^{(d)}$ and $\hat{f}^{(d)}$ are periodic functions with a period of 2π . Thus, it suffices to consider the average variance over $[0, 2\pi)$:

$$h^{(d)}(\mathbf{x}) := \frac{1}{2\pi} \int_0^{2\pi} \operatorname{Var}[\hat{f}^{(d)}(x)] dx = \langle \operatorname{VAR}[\hat{\mathbf{z}}_\mathbf{x}], \mathcal{I}_d \rangle, \quad (48)$$

where the matrix

$$\mathcal{I}_d := \frac{1}{2\pi} \int_0^{2\pi} \mathbf{t}^{(d)}(x) \mathbf{t}^{(d)}(x)^\dagger dx = \begin{cases} \frac{1}{2} I_n, & \text{if } d = 0, \\ \frac{1}{2} \text{Diag}(0, 1, 1, 2^{2d}, 2^{2d}, \dots, r^{2d}, r^{2d}), & \text{if } d \geq 1, \end{cases} \quad (49)$$

is constant with respect to \mathbf{x} . $h^{(d)}(\mathbf{x})$ measures the quality (at an average level) of how well the derivatives of the approximated function estimate the true derivatives. This motivates us to seek interpolation nodes that minimize the value of $h^{(d)}(\mathbf{x})$, leading to the following theorem. For proofs, see Appendix D.5.

Theorem 3 (Minimal Average Variance of Derivatives). *Given any integer $d \geq 0$. When Assumption 2 holds, the $\frac{2\pi}{n}$ -equidistant nodes \mathbf{x}^* with an arbitrary shift value, as defined in Eq. (39), globally solves*

$$\mathbf{x}^* = \underset{\substack{\mathbf{x} \in \mathbb{R}^n \\ x_i \text{ distinct modulo } 2\pi}}{\text{argmin}} h^{(d)}(\mathbf{x}) = \langle \text{VAR}[\hat{\mathbf{z}}_{\mathbf{x}}], \mathcal{I}_d \rangle, \quad (50)$$

where the global minimum is $2\sigma^2$ if $d = 0$, and $\frac{2\sigma^2}{n} \sum_{k=1}^r k^{2d}$ if $d \geq 1$.

For the special case of $d = 0$, Eq. (49) shows that

$$h^{(0)}(\mathbf{x}) = \frac{1}{2} \langle \text{VAR}[\hat{\mathbf{z}}_{\mathbf{x}}], I_n \rangle = \frac{1}{2} \text{MSE}(\hat{\mathbf{z}}_{\mathbf{x}}). \quad (51)$$

This coincides with the problem addressed in Theorem 1 and establishes the same result. An important observation is that the $\frac{2\pi}{n}$ -equidistant nodes constitute the optimal solution \mathbf{x}^* for all $d \geq 0$, but the minimum average variance grows exponentially with respect to d .

Remark 1. *In the case of equidistant frequencies, we find that the $\frac{2\pi}{n}$ -equidistant nodes can simultaneously minimize the three different optimal criteria. However, this result does not hold in the case of general frequencies. In general, minimizing any one of the three criteria, such as the MSE criteria in the OICD algorithm, will also reduce the loss function value of the other criteria, but it cannot achieve the optimality simultaneously.*

4.2 Variance of approximated functions

This subsection analyzes the variance properties of $\hat{f}(x)$ and $\tilde{f}(x)$, showing they share the same variance under specific conditions, and compares the derivative estimators of OICD and PSR, highlighting OICD's computational efficiency by avoiding repeated quantum evaluations. Throughout this subsection, suppose that Assumption 2 holds and we have chosen the $\frac{2\pi}{n}$ -equidistant nodes \mathbf{x}^* . Then, the covariance matrix of $\hat{\mathbf{z}}_{\mathbf{x}}$ becomes $\text{VAR}[\hat{\mathbf{z}}_{\mathbf{x}^*}] = \frac{2\sigma^2}{n} I$. In this case, as shown in Lemma 11 of Appendix D.5, we have (for any $d \geq 0$):

$$\text{Cov}[\hat{f}^{(d)}(x_1), \hat{f}^{(d)}(x_2)] = \frac{2}{n} \sigma^2 \cdot \mathbf{t}^{(d)}(x_1)^\dagger \mathbf{t}^{(d)}(x_2), \quad \forall x_1, x_2 \in \mathbb{R}, \quad (52)$$

$$\text{Var}[\hat{f}^{(d)}(x)] = \frac{2}{n} \sigma^2 \cdot \mathbf{t}^{(d)}(x)^\dagger \mathbf{t}^{(d)}(x), \quad \forall x \in \mathbb{R}. \quad (53)$$

4.2.1 Comparison of function evaluation variance: $\hat{f}(x)$ vs. $\tilde{f}(x)$

By setting $d = 0$ and defining $s := |x_1 - x_2|$, we obtain

$$\text{Cov}[\hat{f}(x_1), \hat{f}(x_2)] = \frac{2}{n} \sigma^2 \left(\frac{1}{2} + \sum_{k=1}^r \cos(ks) \right) = \frac{\sin\left(\frac{n}{2}s\right)}{n \sin\left(\frac{1}{2}s\right)} \sigma^2. \quad (54)$$

Notably, for $x = x_1 = x_2$, we have

$$\text{Var}[f(x)] = \text{Cov}[f(x), f(x)] = \sigma^2, \quad \forall x \in \mathbb{R}. \quad (55)$$

This leads to the assertion that

$$\hat{f}(x) \sim \mathcal{N}(f(x), \sigma^2). \quad (56)$$

Interestingly, this distribution is identical to $\tilde{f}(x) \sim \mathcal{N}(f(x), \sigma^2)$ given in Eq. (25) from Setting I. But, what is the difference? Recall that evaluating $x \mapsto \tilde{f}(x)$ incurs quantum overhead, as it requires numerous measurements after running the quantum circuit. Specifically, when the argument x is modified, the entire process must be repeated from the beginning. Conversely, evaluating $x \mapsto \hat{f}(x)$ for arbitrary x incurs no quantum overhead, as we rely entirely on the approximated function Eq. (113) using a classical computer. It is important to note, however, that $\tilde{f}(x)$ are independent random variables for any two distinct x , which is generally not true for $\hat{f}(x)$. The last equality in Eq. (54) implies that $\text{Cov}[\hat{f}(x_1), \hat{f}(x_2)] = 0$ if and only if $|x_1 - x_2| = \frac{2\pi}{n}k$ for any integer $k \neq 0 \pmod{n}$.

Returning to Algorithm 3, we used $\hat{f}(\theta_k^t)$ to replace $\tilde{f}(\theta_j^t)$ because both are unbiased estimators of $f(\theta^t)$, as shown in Eq. (37) and Eq. (38). This substitution is valid at the algorithmic level. However, we did not previously analyze their variances: the variance of $\tilde{f}(\theta_j^t)$ is σ^2 according to Eq. (25), but the variance of $\hat{f}(\theta_k^t)$ depends on θ_k^t and is difficult to determine. It is typically not exactly equal to σ^2 , meaning their probability distributions are not strictly identical. However, when our PQC problem has equidistant frequencies and we use $\frac{2\pi}{n}$ -equidistant nodes, as shown in Eq. (55), the variance of any point is always σ^2 , which matches the variance of $\tilde{f}(\theta_j^t)$. Therefore, we can theoretically treat the value of $\hat{f}(\theta_k^t)$ as if it were a true sample from $\tilde{f}(\theta_j^t) \sim \mathcal{N}(f(\theta_j^t), \sigma^2)$. At this point, the theory behind the practical OICD Algorithm 3 is fully refined.

4.2.2 Comparison of derivative variance: OICD vs. PSR

In general, for any $d \geq 1$, we have

$$\text{Var}[\hat{f}^{(d)}(x)] = \frac{2}{n}\sigma^2 \cdot \mathbf{t}^{(d)}(x)^\dagger \mathbf{t}^{(d)}(x) = \frac{2}{n}\sigma^2 \sum_{k=1}^r k^{2d}, \quad \forall x \in \mathbb{R}. \quad (57)$$

This result indicates that, with $\frac{2\pi}{n}$ -equidistant interpolation nodes, the quantity above not only represents the minimum average variance as established in Theorem 3, but also provides the same variance across all $x \in \mathbb{R}$. Given the central role of the first-order derivative in optimization, we define the symbols

$$g(x) := \frac{df}{dx}(x) = \mathbf{t}^{(1)}(x)^\dagger \mathbf{z} \quad (58)$$

and

$$g_{\text{oicd}}(x) := \frac{d\hat{f}}{dx}(x) = \mathbf{t}^{(1)}(x)^\dagger \hat{\mathbf{z}}_{\mathbf{x}}. \quad (59)$$

Setting $d = 1$ in Eq. (57) yields

$$\text{Var}[g_{\text{oicd}}(x)] = \frac{2}{n}\sigma^2 \sum_{k=1}^r k^2 = \frac{r(r+1)}{3}\sigma^2, \quad \forall x \in \mathbb{R}. \quad (60)$$

Thus, unbiased g_{oicd} has constant variance across all x .

This reminds us of another approach for unbiasedly estimating the true derivative in PQCs, namely, parameter shift rule (PSR) [30, 31, 20]. We skip the technical details of PSR and focus only on the conclusion; for more see Appendix E. Under the equidistant frequencies in Assumption 2, the PSR [20] employs the following estimator to approximate $g(x)$:

$$g_{\text{psr}}(x) := \sum_{\mu=1}^{2r} \frac{(-1)^{\mu-1}}{4r \sin^2(\frac{1}{2}x_\mu)} \tilde{f}(x + x_\mu), \quad \forall x \in \mathbb{R}, \quad (61)$$

where $x_\mu = \frac{\pi}{2r} + (\mu - 1)\frac{\pi}{r}$ for $\mu = 1, 2, \dots, 2r$. In fact, [20] demonstrated that $\mathbb{E}[g_{\text{psr}}(x)] = g(x)$ and

$$\text{Var}[g_{\text{psr}}(x)] = \sum_{\mu=1}^{2r} \frac{1}{16r^2 \sin^4(\frac{1}{2}x_\mu)} \text{Var}[\tilde{f}(x + x_\mu)] \approx \frac{2r^2 + 1}{6}\sigma^2, \quad \forall x \in \mathbb{R}, \quad (62)$$

where we use the fact that $\tilde{f}(x)$ are independent random variables for any two distinct x , and $\text{Var}[\tilde{f}(x + x_\mu)] \approx \sigma^2$ according to Assumption 1. We can see that both g_{oidc} and g_{psr} serve as unbiased estimators of $g(x)$ for any x . The variance of g_{oidc} is slightly higher than that of g_{psr} , but the difference becomes negligible as $r \rightarrow \infty$.

Notably, g_{oidc} is computed entirely on a classical computer from \hat{f} , which requires a total of $n = 2r + 1$ evaluations of \tilde{f} . Once \hat{f} is available, we can calculate $g_{\text{oidc}}(x)$ for any x without further quantum overhead. In contrast, $g_{\text{psr}}(x)$ requires recalculating \tilde{f} for $2r$ times for each new argument x . Similarly, as before, the unbiased derivatives g_{oidc} at different x values are generally not independent, whereas g_{psr} is typically independent. Overall, although both g_{psr} and g_{oidc} are unbiased estimators of the true g , they are derived from two different techniques: g_{psr} is obtained via the parameter shift rule, while g_{oidc} is derived through interpolation.

5 Numerical simulation

In this section, we use numerical experiments to demonstrate the efficiency of the OICD algorithm.

5.1 Metrics and implementation details

Metrics We use two performance metrics: energy ratio and fidelity. Let E_{ground} and $|\psi_{\text{ground}}\rangle$ denote the true ground energy and ground state of the Hamiltonian, respectively. The energy ratio is defined as

$$\frac{E(\boldsymbol{\theta}^*)}{E_{\text{ground}}}, \quad (63)$$

where $E(\boldsymbol{\theta}) = \langle \psi(\boldsymbol{\theta}) | H | \psi(\boldsymbol{\theta}) \rangle$ is the true expectation value of cost function. The fidelity \mathcal{F} between the optimized state $|\psi(\boldsymbol{\theta}^*)\rangle$ and the true ground state $|\psi_{\text{ground}}\rangle$ is given by

$$\mathcal{F} = |\langle \psi(\boldsymbol{\theta}^*) | \psi_{\text{ground}} \rangle|. \quad (64)$$

Note that for the models studied in this work, $|\psi_{\text{ground}}\rangle$ is always non-degenerate (i.e., the multiplicity of E_{ground} is one). If $\mathcal{F} > 99.9\%$, it implies that we have successfully found the ground state. In fact, if the algorithm converges, both the energy ratio and fidelity will approach 1.

Implementation details To implement the quantum circuits, we used the IBM Qiskit Aer Simulator [32], which simulates the sampling process and the noisy environment of a real machine. All tests were executed on a computer equipped with an AMD Ryzen 7 8845H CPU and 32GB of RAM. The code is publicly available.³

For each function evaluation, we always perform 1000 shots. The initial weights are chosen uniformly from the range $[0, 2\pi]$. We use Algorithm 3 as the implementation of OICD. OICD uses the eigenvalue method (see Appendix F) to exactly solve the subproblem. For OICD and RCD, we randomly select the coordinate index j for updates. For SGD and RCD, we need to compute unbiased derivatives. To this end, we apply the parameter shift rule stated in Appendix E. The learning rates for SGD and RCD are set to 0.01 and 0.02, respectively, yielding reasonably consistent results across all models. In general, the performance of SGD and RCD is highly dependent on the setting of the learning rate, which varies across different problems. In contrast, our OICD method does not require the adjustment of any hyper-parameters.

5.2 Main results

Let N denote the number of qubits, and Pauli matrices are defined as follows

$$\sigma^x \equiv \begin{pmatrix} 0 & 1 \\ 1 & 0 \end{pmatrix}, \quad \sigma^y \equiv \begin{pmatrix} 0 & -i \\ i & 0 \end{pmatrix}, \quad \sigma^z \equiv \begin{pmatrix} 1 & 0 \\ 0 & -1 \end{pmatrix}. \quad (65)$$

The symbol σ_i^α corresponds to a Pauli matrix ($\alpha = x, y, z$) acting on a i -th qubit.

³https://github.com/GALVINLAI/OICD_for_VQA

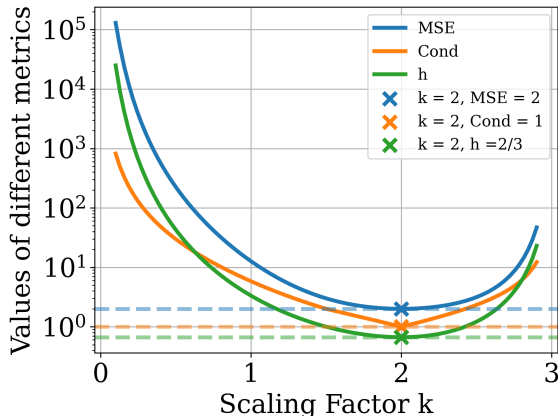


Figure 3: Comparison of the three optimality criteria — mean squared error (MSE), condition number (Cond) and average variance of derivatives (h) (i.e., Theorem 1, Theorem 2, and Theorem 3) — as functions of $k \in (0, 3)$, where the interpolation nodes starting at zero and spaced by $\frac{k\pi}{3}$.

5.2.1 Optimal interpolation nodes is crucial for OICD methods

We use the maxcut problem as an example to illustrate the importance of selecting optimal interpolation nodes for OICD algorithms. For the maxcut problem, we consider the undirected graph $G = (V, E)$ with nodes set $V = \{0, 1, 2, 3\}$ and edge set $E = \{(0, 1), (0, 2), (0, 3), (1, 2), (2, 3)\}$. The goal is to maximize $\sum_{(i,j) \in E} x_i (1 - x_j)$. For the given graph, the Hamiltonian of maxcut problem can be formulated as

$$H = \frac{1}{2}I - 3\sigma_0^z + \frac{1}{2}\sigma_0^z\sigma_1^z + \frac{1}{2}\sigma_0^z\sigma_2^z + \frac{1}{2}\sigma_0^z\sigma_3^z + \frac{1}{2}\sigma_1^z\sigma_2^z + \frac{1}{2}\sigma_2^z\sigma_3^z. \quad (66)$$

Using this Hamiltonian, we construct a hardware-efficient ansatz (HEA) quantum circuit with $N = 4$ and $p = 5$ as in Figure 7 in Appendix G.

From Figure 7, we know that every weight w_j corresponds to the singleton $\Omega = \{1\}$ with $r = 1$ and $n = 3$. We have proved that the $2\pi/3$ -equidistant nodes are the optimal interpolation nodes, i.e., three interpolation nodes each spaced by $2\pi/3$ (without loss of generality, let us assume the starting point is zero). For comparison, we also consider interpolation nodes spaced by $k\pi/3$ with factor $k \in (0, 3)$. Figure 3 illustrates the three optimality criteria from Theorem 1, Theorem 2, and Theorem 3 as functions of k , showing that when $k = 2$, all criteria achieve their minimum values simultaneously. Both too large and too small spacings cause the three criteria to increase.

Figure 4 compares the performance of OICD in solving the maxcut problem under both noisy and noiseless conditions for different sets of interpolation nodes. Theoretically, in the absence of noise, as long as the interpolation nodes are distinct modulo 2π , we can recover the exact coefficients. Hence, in the noiseless case, OICD always successfully solves the problem, as demonstrated in the left panel of Figure 4. However, under noisy conditions, only the optimal interpolation nodes ($k = 2, \text{MSE} = 2$) allow effective convergence. When non-optimal interpolation nodes are used, the variance in the estimated coefficients is too large, causing poor algorithmic performance. As shown in the right panel of Figure 4, when $k = 1$ or $k = 0.5$, the algorithm hardly converges. Even when $k = 1.5$ yields an MSE of 3 — close to the optimal value of 2 — the algorithm still fails to converge in the later stages of iteration. It emphasized that the OICD algorithm is meaningful in practice only when optimal interpolation is applied.

5.2.2 OICD methods outperform than SGD, RCD

Here, we compare the performance of our OICD method (Algorithm 3) with the SGD and RCD methods. We consider the transverse-field Ising model (TFIM) and XXZ model, which are prototypical models for studying quantum magnetism. The details of those models and circuits can be founded in [33].

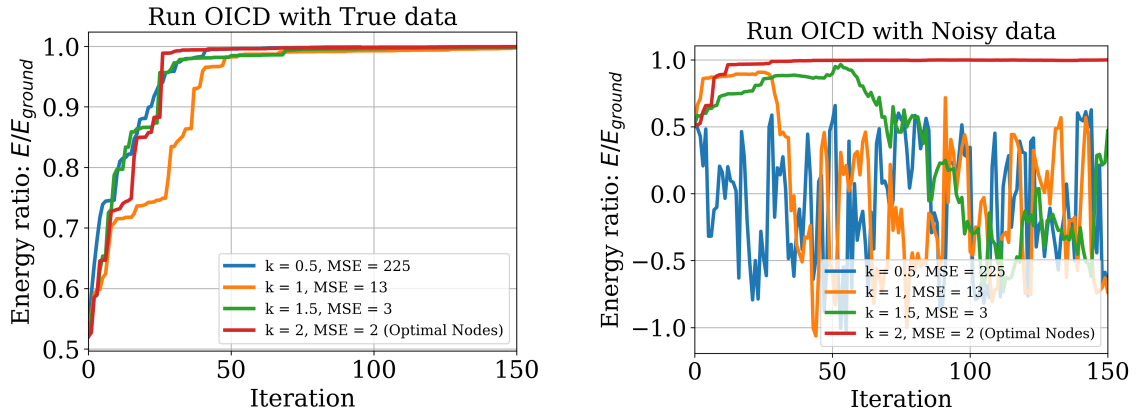


Figure 4: The figures illustrate the performance of the OICD algorithm in solving the maxcut problem under both noisy and noiseless conditions for different sets of interpolation nodes.

TFIM model The Hamiltonian for TFIM is given by

$$H_{\text{TFIM}} = H_{zz} + \Delta H_x \quad (67)$$

where $H_{zz} = \sum_{i=1}^N \sigma_i^z \sigma_{i+1}^z$ and $H_x = \sum_{i=1}^N \sigma_i^x$. Here, we assume that $\Delta > 0$ and use periodic boundary conditions $\sigma_{N+1}^z \equiv \sigma_1^z$. We consider a depth- p Hamiltonian variational ansatz (HVA) circuit for the TFIM that corresponds to

$$U_{\text{TFIM}}(\beta, \gamma) = \prod_{l=1}^p G(\beta_l, H_{zz}) G(\gamma_l, H_x), \quad (68)$$

where $G(x, H) = \exp(-i\frac{x}{2}H)$. Hence, for a depth- p circuit, we have $2p$ parameters. Figure 8 in Appendix G illustrates the quantum circuit for $N = 4$ and $p = 1$. For any N , we observe that every weights β_l, γ_l correspond to the singleton $\Omega = \{2\}$ with $r = 1$ and $n = 3$.

XXZ model The Hamiltonian for XXZ model is given by

$$H_{\text{XXZ}} = H_{xx} + H_{yy} + \Delta H_{zz} \quad (69)$$

where $H_{xx} = \sum_{i=1}^N \sigma_i^x \sigma_{i+1}^x$, $H_{yy} = \sum_{i=1}^N \sigma_i^y \sigma_{i+1}^y$ and $H_{zz} = \sum_{i=1}^N \sigma_i^z \sigma_{i+1}^z$. The parameter $\Delta > 0$ controls the spin anisotropy in the model. Also, we use periodic boundary conditions, i.e., $\sigma_{N+1}^\alpha \equiv \sigma_1^\alpha$ for $\alpha = x, y, z$. A depth- p HVA circuit for the XXZ model corresponds to

$$U_{\text{XXZ}}(\theta, \phi, \beta, \gamma) = \prod_{l=1}^p G(\theta_l, H_{zz}^{\text{odd}}) G(\phi_l, H_{yy}^{\text{odd}}) G(\phi_l, H_{xx}^{\text{odd}}) G(\beta_l, H_{zz}^{\text{even}}) G(\gamma_l, H_{yy}^{\text{even}}) G(\gamma_l, H_{xx}^{\text{even}}), \quad (70)$$

where $G(x, H) = \exp(-i\frac{x}{2}H)$, $H_{\alpha\alpha}^{\text{even}} = \sum_{i=1}^{N/2} \sigma_{2i-1}^\alpha \sigma_{2i}^\alpha$ and $H_{\alpha\alpha}^{\text{odd}} = \sum_{i=1}^{N/2} \sigma_{2i}^\alpha \sigma_{2i+1}^\alpha$ for $\alpha = x, y, z$. Hence for a depth- p circuit, we have $4p$ parameters. Figure 9 in Appendix G illustrates a quantum circuit for $N = 6$ and $p = 1$. In the case of $N = 6$, we observe that the weights θ_l, β_l correspond to the $\Omega = \{2\}$ with $r = 1$ and $n = 3$, while the weights ϕ_l, γ_l correspond to the $\Omega = \{2, 4\}$ with $r = 2$ and $n = 5$.

The performance comparisons of OICD, SGD, and RCD in optimizing the Hamiltonian for the TFIM and XXZ models are shown in Figure 5 and Figure 6, respectively. The x -axis represents the number of function evaluations, indicating the quantum overhead. For each model, we conducted the experiment 10 times, using different random initializations for each run, but all methods started from the same initial points. For each method, we plot the mean values against the corresponding number of function evaluations. The shaded area represents the fluctuation within one standard deviation above and below the mean. All the results in Figure 5 and Figure 6 show that OICD can find the optimal solution with significantly fewer function evaluations compared to SGD and RCD. This clearly demonstrates the high efficiency of the OICD algorithm.

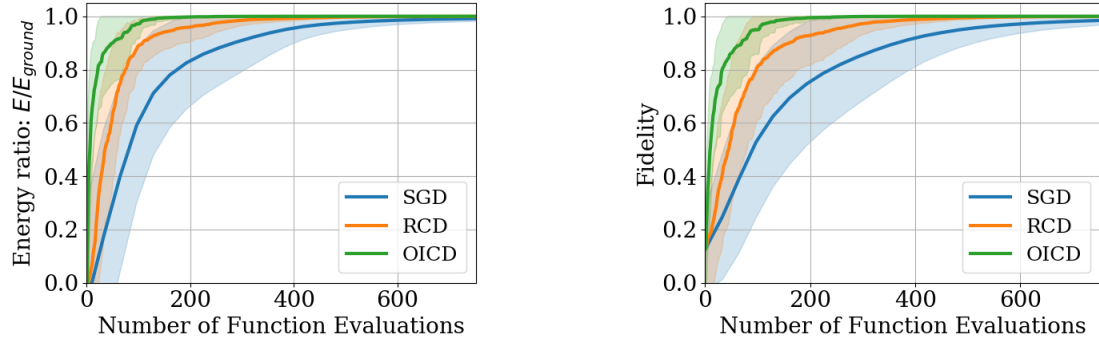


Figure 5: The performance comparison of OICD, SGD, and RCD for the TFIM model with $\Delta = 0.5$, where $N = 6$ and $p = 8$. The figures display the ground state approximation, with the energy ratio on the left and fidelity on the right.

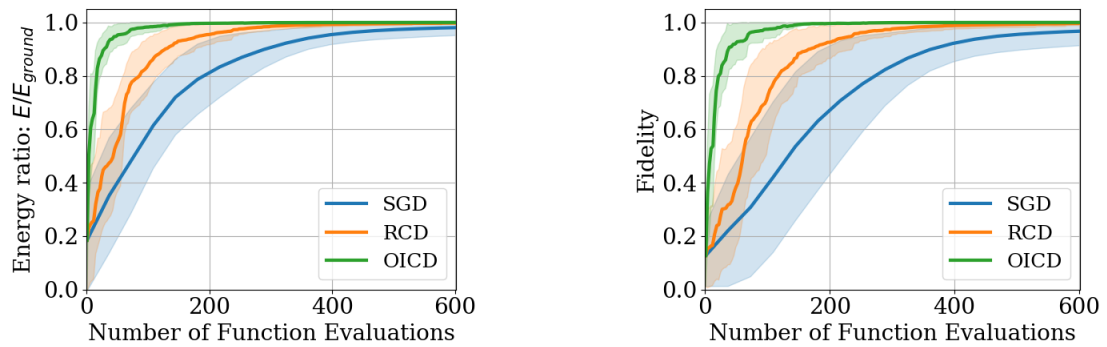


Figure 6: The performance comparison of OICD, SGD, and RCD for the XXZ model with $\Delta = 0.5$, where $N = 6$ and $p = 3$. The figures display the ground state approximation, with the energy ratio on the left and fidelity on the right.

6 Discussion

In this work, we present an optimal interpolation-based coordinate descent (OICD) method to solve the classical optimization problem in parameterized quantum circuits. By incorporating interpolation techniques, the OICD method significantly improves computational efficiency. The use of trigonometric polynomial models enables effective approximation of the cost function, while the careful selection of interpolation nodes helps minimize the impact of noise in quantum measurements. For equidistant frequencies case, we showed that using $\frac{2\pi}{n}$ -equidistant nodes is an optimal strategy, meeting three different criteria simultaneously. Overall, the OICD method demonstrates improved optimization performance for PQCs, combining enhanced descent properties with efficient noise management, making it a promising tool for quantum-classical hybrid optimization tasks. Below, we discuss several promising future works to conclude this paper.

Noise stability and robustness Understanding the impact of noise on the stability of OICD is an important direction. Since noise is inherent in quantum systems, it is crucial to analyze how it affects the solution of the approximated subproblem. As discussed in Appendix F, the eigenvalue-based method for solving subproblems with equidistant frequencies allows us to establish an exact map relation between estimated coefficients and the final solution. This suggests that a rigorous stability analysis is feasible, albeit challenging, and could provide deeper insights into the resilience of OICD under realistic quantum conditions.

Sparsity in the Fourier series Our experiments reveal that the Fourier series representation of $f(\theta_j)$ often exhibits sparsity, with the scale of r_j depending on the ansatz, Hamiltonian, and boundary conditions. For instance, in the case of the TFIM model with an HVA ansatz, as discussed in Section 5.2.2, we consistently observe $r_j = 1$ for all coordinates j , regardless of the number of layers or qubits. However, in general, this sparsity structure may require a case-by-case analysis. Identifying and exploiting such sparsity could significantly reduce the number of samples required for interpolation, thereby enhancing the efficiency of OICD.

Convergence theory of OICD The theoretical convergence properties of OICD remain an open question. Unlike standard coordinate descent (CD) algorithms, OICD does not have a direct counterpart in classical optimization literature, primarily because existing convergence results for CD algorithms typically assume noise-free cost functions. While some CD algorithms update each step using argmin, they do not account for noise in their problems. OICD may introduce a new optimization formulation, requiring a tailored theoretical analysis to establish its convergence properties. Investigating this aspect is an important direction for future research.

Acknowledgments

This work was supported by the National Natural Science Foundation of China under the grant numbers 12331010 and 12288101, and the National Key R&D Program of China under the grant number 2024YFA1012903. We would like to express our sincere gratitude to Liyuan Cao, Zhiyan Ding, Tianyou Li, Xiantao Li, Xiufan Li, Lin Lin, Yin Liu, and Zaiwen Wen for their valuable feedback and insightful comments on the manuscript.

References

- [1] Marco Cerezo, Andrew Arrasmith, Ryan Babbush, Simon C Benjamin, Suguru Endo, Keisuke Fujii, Jarrod R McClean, Kosuke Mitarai, Xiao Yuan, Lukasz Cincio, et al. “Variational quantum algorithms”. *Nature Reviews Physics* **3**, 625–644 (2021).
- [2] Nikolaj Moll, Panagiotis Barkoutsos, Lev S Bishop, Jerry M Chow, Andrew Cross, Daniel J Egger, Stefan Filipp, Andreas Fuhrer, Jay M Gambetta, Marc Ganzhorn, et al. “Quantum optimization using variational algorithms on near-term quantum devices”. *Quantum Science and Technology* **3**, 030503 (2018).

- [3] Alberto Peruzzo, Jarrod McClean, Peter Shadbolt, Man-Hong Yung, Xiao-Qi Zhou, Peter J Love, Alán Aspuru-Guzik, and Jeremy L O’Brien. “A variational eigenvalue solver on a photonic quantum processor”. *Nature communications* **5**, 4213 (2014).
- [4] Abhinav Kandala, Antonio Mezzacapo, Kristan Temme, Maika Takita, Markus Brink, Jerry M Chow, and Jay M Gambetta. “Hardware-efficient variational quantum eigensolver for small molecules and quantum magnets”. *nature* **549**, 242–246 (2017).
- [5] Harper R Grimsley, Sophia E Economou, Edwin Barnes, and Nicholas J Mayhall. “An adaptive variational algorithm for exact molecular simulations on a quantum computer”. *Nature communications* **10**, 3007 (2019).
- [6] Zhong-Xia Shang, Ming-Cheng Chen, Xiao Yuan, Chao-Yang Lu, and Jian-Wei Pan. “Schrödinger-heisenberg variational quantum algorithms”. *Phys. Rev. Lett.* **131**, 060406 (2023).
- [7] Xiao Yuan, Suguru Endo, Qi Zhao, Ying Li, and Simon C. Benjamin. “Theory of variational quantum simulation”. *Quantum* **3**, 191 (2019).
- [8] Sam McArdle, Tyson Jones, Suguru Endo, Ying Li, Simon C. Benjamin, and Xiao Yuan. “Variational ansatz-based quantum simulation of imaginary time evolution”. *npj Quantum Information* **5**, 75 (2019).
- [9] Suguru Endo, Jinzhao Sun, Ying Li, Simon C. Benjamin, and Xiao Yuan. “Variational quantum simulation of general processes”. *Phys. Rev. Lett.* **125**, 010501 (2020).
- [10] Edward Farhi, Jeffrey Goldstone, and Sam Gutmann. “A quantum approximate optimization algorithm” (2014).
- [11] Leo Zhou, Sheng-Tao Wang, Soonwon Choi, Hannes Pichler, and Mikhail D Lukin. “Quantum approximate optimization algorithm: Performance, mechanism, and implementation on near-term devices”. *Physical Review X* **10**, 021067 (2020).
- [12] Kostas Blekos, Dean Brand, Andrea Ceschini, Chiao-Hui Chou, Rui-Hao Li, Komal Pandya, and Alessandro Summer. “A review on quantum approximate optimization algorithm and its variants”. *Physics Reports* **1068**, 1–66 (2024).
- [13] Maria Schuld and Nathan Killoran. “Quantum machine learning in feature hilbert spaces”. *Physical review letters* **122**, 040504 (2019).
- [14] Vojtěch Havlíček, Antonio D Córcoles, Kristan Temme, Aram W Harrow, Abhinav Kandala, Jerry M Chow, and Jay M Gambetta. “Supervised learning with quantum-enhanced feature spaces”. *Nature* **567**, 209–212 (2019).
- [15] Maria Schuld, Alex Bocharov, Krysta M Svore, and Nathan Wiebe. “Circuit-centric quantum classifiers”. *Physical Review A* **101**, 032308 (2020).
- [16] Alejandro Perdomo-Ortiz, Marcello Benedetti, John Realpe-Gómez, and Rupak Biswas. “Opportunities and challenges for quantum-assisted machine learning in near-term quantum computers”. *Quantum Science and Technology* **3**, 030502 (2018).
- [17] Nathan Killoran, Thomas R Bromley, Juan Miguel Arrazola, Maria Schuld, Nicolás Quesada, and Seth Lloyd. “Continuous-variable quantum neural networks”. *Physical Review Research* **1**, 033063 (2019).
- [18] Marcello Benedetti, Erika Lloyd, Stefan Sack, and Mattia Fiorentini. “Parameterized quantum circuits as machine learning models”. *Quantum Science and Technology* **4**, 043001 (2019).
- [19] Ryan Sweke, Frederik Wilde, Johannes Meyer, Maria Schuld, Paul K Fährmann, Barthélémy Meynard-Piganeau, and Jens Eisert. “Stochastic gradient descent for hybrid quantum-classical optimization”. *Quantum* **4**, 314 (2020).
- [20] David Wierichs, Josh Izaac, Cody Wang, and Cedric Yen-Yu Lin. “General parameter-shift rules for quantum gradients”. *Quantum* **6**, 677 (2022).
- [21] Andrea Mari, Thomas R Bromley, and Nathan Killoran. “Estimating the gradient and higher-order derivatives on quantum hardware”. *Physical Review A* **103**, 012405 (2021).
- [22] Zhiyan Ding, Taehee Ko, Jiahao Yao, Lin Lin, and Xiantao Li. “Random coordinate descent: a simple alternative for optimizing parameterized quantum circuits”. *Physical Review Research* **6**, 033029 (2024).
- [23] Gavin E Crooks. “Gradients of parameterized quantum gates using the parameter-shift rule and gate decomposition” (2019).

- [24] John P Boyd. “Computing the zeros, maxima and inflection points of chebyshev, legendre and fourier series: solving transcendental equations by spectral interpolation and polynomial rootfinding”. *Journal of Engineering Mathematics* **56**, 203–219 (2006).
- [25] Michael A Nielsen and Isaac L Chuang. “Quantum computation and quantum information”. *Cambridge university press*. (2010).
- [26] Liubov Markovich, Savvas Malikis, Stefano Polla, and Jordi Tura. “Parameter shift rule with optimal phase selection”. *Physical Review A* **109**, 062429 (2024).
- [27] Hao-Jun Michael Shi, Shenyinying Tu, Yangyang Xu, and Wotao Yin. “A primer on coordinate descent algorithms” (2016).
- [28] Mateusz Ostaszewski, Edward Grant, and Marcello Benedetti. “Structure optimization for parameterized quantum circuits”. *Quantum* **5**, 391 (2021).
- [29] Lloyd N. Trefethen and David Bau. “Numerical linear algebra, twenty-fifth anniversary edition”. *Society for Industrial and Applied Mathematics*. Philadelphia, PA (2022). [arXiv:https://epubs.siam.org/doi/pdf/10.1137/1.9781611977165](https://epubs.siam.org/doi/pdf/10.1137/1.9781611977165).
- [30] Jun Li, Xiaodong Yang, Xinhua Peng, and Chang-Pu Sun. “Hybrid quantum-classical approach to quantum optimal control”. *Physical review letters* **118**, 150503 (2017).
- [31] Maria Schuld, Ville Bergholm, Christian Gogolin, Josh Izaac, and Nathan Killoran. “Evaluating analytic gradients on quantum hardware”. *Physical Review A* **99**, 032331 (2019).
- [32] Qiskit Community. “Qiskit: An open-source framework for quantum computing” (2017).
- [33] Roeland Wiersema, Cunlu Zhou, Yvette de Sereville, Juan Felipe Carrasquilla, Yong Baek Kim, and Henry Yuen. “Exploring entanglement and optimization within the hamiltonian variational ansatz”. *PRX quantum* **1**, 020319 (2020).

A Trigonometric representation of PQC cost function

The derivation of Eq. (11) comes from [20]. For the sake of completeness, we provide the detailed derivation process in this appendix. We begin by formulating a PQC cost function that depends on a single parameter $x \in \mathbb{R}$. Consider the unitary defined as

$$U(x) = \exp(iHx), \quad (71)$$

where H is a Hermitian generator. Let $|\psi\rangle$ denote the quantum state to which $U(x)$ is applied, and let B represent the observable being measured. The PQC cost function is then defined by

$$f(x) := \langle \psi | U(x)^\dagger B U(x) | \psi \rangle. \quad (72)$$

Let $\{\lambda_j\}_{j \in [N]}$ represent the eigenvalues of H , where $[N] := \{1, \dots, N\}$ and the eigenvalues are arranged in non-decreasing order ($\lambda_1 \leq \dots \leq \lambda_N$). For any real number x , the set $\{\exp(i\lambda_j x)\}_{j \in [N]}$ constitutes the eigenvalues of $U(x)$. Specifically, let $\{|\phi_j\rangle\}_{j \in [N]}$ be the eigenbasis of H . Then, H can be diagonalized as

$$H = \sum_{j=1}^N \lambda_j |\phi_j\rangle \langle \phi_j|, \quad (73)$$

and $U(x) = \exp(iHx)$ can also be diagonalized in the same eigenbasis as

$$U(x) = \sum_{j=1}^N \exp(ix\lambda_j) |\phi_j\rangle \langle \phi_j|. \quad (74)$$

We proceed by expanding B and $|\psi\rangle$ in the eigenbasis $\{|\phi_j\rangle\}_{j \in [N]}$. Specifically, we define the matrix entries of B and the coefficients of $|\psi\rangle$ in this eigenbasis by

$$b_{jk} := \langle \phi_j | B | \phi_k \rangle, \quad \psi_j := \langle \phi_j | \psi \rangle, \quad \forall j, k \in [N]. \quad (75)$$

By Eq. (74), we apply $U(x)$ to the state $|\psi\rangle$ to obtain

$$U(x)|\psi\rangle = \sum_{j=1}^N \exp(ix\lambda_j) |\phi_j\rangle \langle \phi_j | \psi \rangle = \sum_{j=1}^N \psi_j \exp(ix\lambda_j) |\phi_j\rangle. \quad (76)$$

Substituting the expanded form of $U(x)|\psi\rangle$ above into $f(x)$, we have

$$f(x) = \langle \psi | U(x)^\dagger B U(x) | \psi \rangle = \left(\sum_{j=1}^N \overline{\psi_j} \exp(-ix\lambda_j) \langle \phi_j | \right) B \left(\sum_{k=1}^N \psi_k \exp(ix\lambda_k) |\phi_k\rangle \right) \quad (77)$$

$$= \sum_{j,k=1}^N \overline{\psi_j} \psi_k \exp[i(\lambda_k - \lambda_j)x] \langle \phi_j | B | \phi_k \rangle \quad (78)$$

$$= \sum_{j,k=1}^N \overline{\psi_j} \psi_k b_{jk} e^{i(\lambda_k - \lambda_j)x}. \quad (79)$$

To further simplify $f(x)$, we separate the terms where $j \neq k$ and $j = k$ and obtain

$$f(x) = \sum_{\substack{j,k=1 \\ j < k}}^N \left[\overline{\psi_j} \psi_k b_{jk} e^{i(\lambda_k - \lambda_j)x} + \psi_j \overline{\psi_k} b_{jk} e^{-i(\lambda_k - \lambda_j)x} \right] + \sum_{j=1}^N |\psi_j|^2 b_{jj}. \quad (80)$$

We can collect the x -independent terms into coefficients defined by $c_{jk} := \overline{\psi_j} \psi_k b_{jk}$. Then, $f(x)$ becomes

$$f(x) = \sum_{\substack{j,k=1 \\ j < k}}^N \left[c_{jk} e^{i(\lambda_k - \lambda_j)x} + \overline{c_{jk}} e^{-i(\lambda_k - \lambda_j)x} \right] + \sum_{j=1}^N |\psi_j|^2 b_{jj}. \quad (81)$$

Moreover, we introduce the unique positive differences

$$\{\Omega_\ell\}_{\ell \in [r]} := \{\lambda_k - \lambda_j \mid \forall j, k \in [N], \lambda_k > \lambda_j\}. \quad (82)$$

Here, r is the number of the unique positive differences. For the same term $e^{i(\lambda_k - \lambda_j)x} = e^{i\Omega_\ell x}$, we sum the coefficients c_{jk} in front of them and re-index it as c_ℓ . Consequently, Eq. (81) becomes

$$f(x) = \sum_{\ell=1}^r c_\ell e^{i\Omega_\ell x} + \sum_{\ell=1}^r \bar{c}_\ell e^{-i\Omega_\ell x} + \sum_{j=1}^N |\psi_j|^2 b_{jj}. \quad (83)$$

Next, we parameterize the complex coefficients c_ℓ by real numbers a_ℓ and b_ℓ as

$$c_\ell = \frac{1}{2}(a_\ell - ib_\ell), \quad \forall \ell \in [r], \quad (84)$$

and define $a_0 := \sqrt{2} \sum_{j=1}^N |\psi_j|^2 b_{jj}$. Notice that b_{jj} must be real since B is Hermitian. Utilizing the trigonometric identities $\cos(x) = \frac{1}{2}(e^{ix} + e^{-ix})$, $\sin(x) = \frac{i}{2}(-e^{ix} + e^{-ix})$, we can rewrite $f(x)$ as a finite-term Fourier series

$$f(x) = \sum_{\ell=1}^r \frac{1}{2}(a_\ell - ib_\ell)e^{i\Omega_\ell x} + \sum_{\ell=1}^r \frac{1}{2}(a_\ell + ib_\ell)e^{-i\Omega_\ell x} + \frac{1}{\sqrt{2}}a_0 \quad (85)$$

$$= \sum_{\ell=1}^r a_\ell \left(\frac{e^{i\Omega_\ell x} + e^{-i\Omega_\ell x}}{2} \right) + \sum_{\ell=1}^r ib_\ell \left(\frac{-e^{i\Omega_\ell x} + e^{-i\Omega_\ell x}}{2} \right) + \frac{1}{\sqrt{2}}a_0 \quad (86)$$

$$= \frac{1}{\sqrt{2}}a_0 + \sum_{\ell=1}^r [a_\ell \cos(\Omega_\ell x) + b_\ell \sin(\Omega_\ell x)], \quad (87)$$

where the frequencies are given by Eq. (82). We complete the proof for equation Eq. (11).

B Recover the complex coefficients of restricted univariate functions

In Section 3.2, we discussed the interpolation method to recover $n = 2r + 1$ real coefficients in the restricted univariate function $f(x)$ in Eq. (20). In this appendix, we discuss an interpolation method for recovering complex coefficients of $f(x)$. It will not appear in our actual OICD algorithms, but it is very useful for explaining the theoretical phenomena behind the OICD. For the moment, assume that we can access to $f(x)$ without noise.

As we saw in Appendix A, there is an alternative equivalent expression for $f(x)$, since we observe that

$$f(x) = \frac{1}{\sqrt{2}}a_0 + \sum_{k=1}^r [a_k \cos(\Omega_k x) + b_k \sin(\Omega_k x)] \quad (88)$$

$$= \frac{1}{\sqrt{2}}a_0 + \sum_{k=1}^r \left[a_k \frac{1}{2} (e^{i\Omega_k x} + e^{-i\Omega_k x}) + b_k \frac{i}{2} (e^{-i\Omega_k x} - e^{i\Omega_k x}) \right] \quad (89)$$

$$= \frac{1}{\sqrt{2}}a_0 + \sum_{k=1}^r \left[\left(\frac{a_k}{2} - \frac{b_k}{2}i \right) e^{i\Omega_k x} + \left(\frac{a_k}{2} + \frac{b_k}{2}i \right) e^{-i\Omega_k x} \right] \quad (90)$$

$$= \sum_{k=-r}^r c_k e^{i\Omega_k x}, \quad (91)$$

where we define $\Omega_{-k} := -\Omega_k$ for $k = 1, \dots, r$ and $\Omega_0 := 0$; and we convert the real coefficients $\mathbf{z} = [a_0, a_1, b_1, \dots, a_r, b_r]^\dagger \in \mathbb{R}^n$ to the complex coefficients

$$\mathbf{z}^c := [c_{-r}, \dots, c_0, \dots, c_r]^\dagger \in \mathbb{C}^n \quad (92)$$

by using the a linear transformation, i.e.,

$$\begin{cases} c_0 := \frac{1}{\sqrt{2}}a_0 \\ c_k := \frac{a_k}{2} - \frac{b_k}{2}i, \forall k = 1, \dots, r \\ c_{-k} := \frac{a_k}{2} + \frac{b_k}{2}i = c_k^*, \forall k = 1, \dots, r \end{cases} \iff \begin{cases} a_0 = \sqrt{2}c_0 \\ a_k = c_k + c_{-k}, \forall k = 1, \dots, r \\ b_k = i(c_k - c_{-k}), \forall k = 1, \dots, r. \end{cases} \quad (93)$$

The invertibility of this transformation establishes the equivalence between the real-coefficient expression Eq. (20) and its complex-coefficient counterpart Eq. (91). If we define the constant matrix

$$C := \begin{bmatrix} & & & & \frac{1}{2} & \frac{i}{2} \\ & & & & \ddots & \\ & & & & & \ddots \\ & & \frac{1}{2} & \frac{i}{2} & & \\ \frac{1}{\sqrt{2}} & & & & & \\ & & \frac{1}{2} & -\frac{i}{2} & & \\ & & & \ddots & & \\ & & & & \frac{1}{2} & -\frac{i}{2} \end{bmatrix} \in \mathbb{C}^{n \times n}, \quad (94)$$

we can rewrite this transformation as $\mathbf{z}^c = C\mathbf{z}$. It is easily to see that $CC^\dagger = C^\dagger C = \frac{1}{2}I$.

Next, like interpolation equation Eq. (24), we also attempt to recover the complex coefficients \mathbf{z}^c by interpolation. Similarly, after selecting some interpolation nodes $\mathbf{x} = [x_0, x_1, \dots, x_{2r}]^\dagger \in \mathbb{R}^n$ with distinct entries, we construct the complex interpolation matrix

$$A_{\mathbf{x}}^c := \begin{bmatrix} \omega_0^{-\Omega_r} & \dots & \omega_0^{-\Omega_1} & 1 & \omega_0^{\Omega_1} & \dots & \omega_0^{\Omega_r} \\ \omega_1^{-\Omega_r} & \dots & \omega_1^{-\Omega_1} & 1 & \omega_1^{\Omega_1} & \dots & \omega_1^{\Omega_r} \\ \vdots & \ddots & \vdots & \vdots & \vdots & \ddots & \vdots \\ \omega_{2r}^{-\Omega_r} & \dots & \omega_{2r}^{-\Omega_1} & 1 & \omega_{2r}^{\Omega_1} & \dots & \omega_{2r}^{\Omega_r} \end{bmatrix} \in \mathbb{C}^{n \times n}, \quad (95)$$

where $\omega_k := e^{ix_k}$ for $k = 0, 1, \dots, 2r$. Then, similarly, we can solve the linear equation

$$A_{\mathbf{x}}^c \mathbf{z}^c = \mathbf{y}_{\mathbf{x}} \quad (96)$$

to obtain \mathbf{z}^c . Notice that $\mathbf{y}_{\mathbf{x}}$ above is again the true data vector given in Eq. (22).

A close relationship exists between real-coefficient and complex-coefficient interpolation schemes. In fact, we have the decomposition $A_{\mathbf{x}}^c = D_{\mathbf{x}}V_{\mathbf{x}}$, where the diagonal matrix (with $\omega_k \equiv e^{ix_k}$)

$$D_{\mathbf{x}} := \text{Diag}(\omega_0^{-\Omega_r}, \omega_1^{-\Omega_r}, \dots, \omega_{2r}^{-\Omega_r}) \in \mathbb{C}^{n \times n} \quad (97)$$

is unitary, and

$$V_{\mathbf{x}} := \begin{bmatrix} 1 & \omega_0^{\Omega_r - \Omega_{r-1}} & \dots & \omega_0^{\Omega_r - \Omega_1} & \omega_0^{\Omega_r} & \omega_0^{\Omega_r + \Omega_1} & \dots & \omega_0^{2\Omega_r} \\ 1 & \omega_1^{\Omega_r - \Omega_{r-1}} & \dots & \omega_1^{\Omega_r - \Omega_1} & \omega_1^{\Omega_r} & \omega_1^{\Omega_r + \Omega_1} & \dots & \omega_1^{2\Omega_r} \\ \vdots & \vdots & \ddots & \vdots & \vdots & \ddots & \vdots & \vdots \\ 1 & \omega_{2r}^{\Omega_r - \Omega_{r-1}} & \dots & \omega_{2r}^{\Omega_r - \Omega_1} & \omega_{2r}^{\Omega_r} & \omega_{2r}^{\Omega_r + \Omega_1} & \dots & \omega_{2r}^{2\Omega_r} \end{bmatrix} \in \mathbb{C}^{n \times n}, \quad (98)$$

which becomes the Vandermonde matrix for equidistant frequencies $\Omega_k = k$ for $k = 1, \dots, r$. The relationship between the real interpolation matrix $A_{\mathbf{x}}$ in Eq. (23) and all the previously defined matrices is as follows:

$$A_{\mathbf{x}} = A_{\mathbf{x}}^c C = D_{\mathbf{x}} V_{\mathbf{x}} C. \quad (99)$$

Since $D_{\mathbf{x}}$ and C are always invertible, $A_{\mathbf{x}}$ is invertible if and only if $V_{\mathbf{x}}$ is invertible. When equidistant frequencies $\Omega_k = k$ for $k = 1, \dots, r$, hold, we can derive the well-known Vandermonde determinant:

$$\det(V_{\mathbf{x}}) = \prod_{0 \leq j < k \leq n} (\omega_k - \omega_j) = \prod_{0 \leq j < k \leq n} (e^{ix_k} - e^{ix_j}), \quad (100)$$

which is non-zero if and only if all x_i are distinct modulo 2π . Therefore, the equation Eq. (24) (also Eq. (96)) always has the unique solution. However, for general Ω_k , it is difficult to find a similar conclusion.

In our OICD algorithms, we only need to use the matrix $A_{\mathbf{x}}$ to recover the real coefficients \mathbf{z} , but the complex coefficient counterpart is very convenient for theoretical analysis. For example, Lemma 1 in Appendix C is a typical instance.

C Detailed explanation behind Practical OICD Algorithm 3

The improvement in the practical OICD Algorithm 3 is based on the following two observations. In this appendix, we give the detailed explanation behind the practical OICD Algorithm 3.

C.1 Observation I: shift invariance of interpolations

We return to the notations used in Section 3.2 and omit the specific index j . We formally state the shift invariance of interpolations in the next lemma.

Lemma 1. *Fix some $\mathbf{x} \in \mathbb{R}^n$ and let $\mathbf{1} \in \mathbb{R}^n$ denotes the all-ones vector. Then, for any shift value $s \in \mathbb{R}$, we have:*

1. $A_{\mathbf{x}+s\mathbf{1}}^{-1} = E_s^{-1} A_{\mathbf{x}}^{-1}$ where the block diagonal matrix $E_s^{-1} = \text{diag}(1, B_1^\dagger, \dots, B_r^\dagger) \in \mathbb{R}^{n \times n}$ and $B_i \in \mathbb{R}^{2 \times 2}$ is given by

$$B_i := \begin{bmatrix} \cos(\Omega_i s) & \sin(\Omega_i s) \\ -\sin(\Omega_i s) & \cos(\Omega_i s) \end{bmatrix}; \quad (101)$$

2. $\|A_{\mathbf{x}+s\mathbf{1}}^{-1}\|_F^2 \equiv \|A_{\mathbf{x}}^{-1}\|_F^2$.

Proof. Let us now construct the matrices corresponding to the shifted interpolation nodes $\mathbf{x} + s\mathbf{1}$. First, we have (with $\omega_k \equiv e^{ix_k}$)

$$V_{\mathbf{x}+s\mathbf{1}} = \begin{bmatrix} 1 & e^{is(\Omega_r - \Omega_{r-1})} \omega_0^{\Omega_r - \Omega_{r-1}} & e^{is(\Omega_r - \Omega_{r-2})} \omega_0^{\Omega_r - \Omega_{r-2}} & \dots & e^{is2\Omega_r} \omega_0^{2\Omega_r} \\ 1 & e^{is(\Omega_r - \Omega_{r-1})} \omega_1^{\Omega_r - \Omega_{r-1}} & e^{is(\Omega_r - \Omega_{r-2})} \omega_1^{\Omega_r - \Omega_{r-2}} & \dots & e^{is2\Omega_r} \omega_1^{2\Omega_r} \\ \vdots & \vdots & \vdots & \ddots & \vdots \\ 1 & e^{is(\Omega_r - \Omega_{r-1})} \omega_{2r}^{\Omega_r - \Omega_{r-1}} & e^{is(\Omega_r - \Omega_{r-2})} \omega_{2r}^{\Omega_r - \Omega_{r-2}} & \dots & e^{is2\Omega_r} \omega_{2r}^{2\Omega_r} \end{bmatrix}. \quad (102)$$

We can observe that $V_{\mathbf{x}+s\mathbf{1}} = V_{\mathbf{x}} S$, where $S \in \mathbb{C}^{n \times n}$ is the diagonal matrix

$$S := \text{Diag}(1, e^{is(\Omega_r - \Omega_{r-1})}, e^{is(\Omega_r - \Omega_{r-2})}, \dots, e^{is2\Omega_r}). \quad (103)$$

Next, we have

$$D_{\mathbf{x}+s\mathbf{1}} = \text{Diag}(e^{-is\Omega_r} \omega_0^{-\Omega_r}, e^{-is\Omega_r} \omega_1^{-\Omega_r}, \dots, e^{-is\Omega_r} \omega_{2r}^{-\Omega_r}) = e^{-is\Omega_r} \cdot D_{\mathbf{x}}. \quad (104)$$

Finally, using the identity $CC^\dagger = \frac{1}{2}I$, we obtain

$$A_{\mathbf{x}+s\mathbf{1}} = D_{\mathbf{x}+s\mathbf{1}} V_{\mathbf{x}+s\mathbf{1}} C = (e^{-is\Omega_r} \cdot D_{\mathbf{x}})(V_{\mathbf{x}} S) C = 2e^{-is\Omega_r} \cdot (D_{\mathbf{x}} V_{\mathbf{x}} C) C^\dagger S C. \quad (105)$$

Since $A_{\mathbf{x}} = D_{\mathbf{x}} V_{\mathbf{x}} C$, we get

$$A_{\mathbf{x}+s\mathbf{1}} = A_{\mathbf{x}} (2e^{-is\Omega_r} \cdot C^\dagger S C) = A_{\mathbf{x}} E_s, \quad (106)$$

where $S' := e^{-is\Omega_r} \cdot S = \text{Diag}(e^{-is\Omega_r}, \dots, e^{-is\Omega_1}, 1, e^{is\Omega_1}, \dots, e^{is\Omega_r})$ is unitary, and

$$E_s := 2C^\dagger S' C. \quad (107)$$

In fact, after substituting the specific expression Eq. (94) for C , E_s can be expressed as a block diagonal matrix given by

$$E_s = \text{Diag}(1, B_1, \dots, B_r) \in \mathbb{R}^{n \times n} \quad (108)$$

where B_i is defined as in Eq. (101). Since each B_i is a rotation matrix, we know that $B_i^{-1} = B_i^\dagger$, so

$$E_s^{-1} = 2C^\dagger(S')^{-1}C = \text{Diag}\left(1, B_1^\dagger, \dots, B_r^\dagger\right). \quad (109)$$

This proves item 1 of Lemma 1. On the other hand,

$$\begin{aligned} \|A_{\mathbf{x}+s\mathbf{1}}^{-1}\|_F^2 &= \text{tr}\left[(A_{\mathbf{x}+s\mathbf{1}}^{-1})^\dagger A_{\mathbf{x}+s\mathbf{1}}^{-1}\right] \\ &= \text{tr}\left[(A_{\mathbf{x}}^{-1})^\dagger (E_s^{-1})^\dagger E_s^{-1} A_{\mathbf{x}}^{-1}\right] \quad (\text{using } A_{\mathbf{x}+s\mathbf{1}} = A_{\mathbf{x}}E_s) \\ &= \text{tr}\left[(A_{\mathbf{x}}^{-1})^\dagger \left(2C^\dagger(S')^{-1}C\right)^\dagger 2C^\dagger(S')^{-1}CA_{\mathbf{x}}^{-1}\right] \\ &= \text{tr}\left[(A_{\mathbf{x}}^{-1})^\dagger \left(4C^\dagger S' C C^\dagger (S')^{-1}C\right) A_{\mathbf{x}}^{-1}\right] \\ &= \text{tr}\left[(A_{\mathbf{x}}^{-1})^\dagger A_{\mathbf{x}}^{-1}\right] = \|A_{\mathbf{x}}^{-1}\|_F^2. \quad (\text{since } S' \text{ is unitary, } CC^\dagger = C^\dagger C = \frac{1}{2}I) \end{aligned} \quad (110)$$

This completes the proof of item 2 of Lemma 1. \square

The second claim in Lemma 1 states that the value of $\|A_{\mathbf{x}}^{-1}\|_F^2$ is invariant under any shift of the fixed vector \mathbf{x} . As a result, if a solution $\mathbf{x}^* = [x_0^*, x_1^*, \dots, x_{2r}^*]^\dagger \in \mathbb{R}^n$ solves Eq. (34), then any shifted vector $\mathbf{x}^* + s\mathbf{1} \in \mathbb{R}^n$ is also a solution. This implies that for $\text{MSE}(\hat{\mathbf{z}}_{\mathbf{x}})$, the key is the spacing between the interpolation nodes, rather than their absolute positions. Consequently, we are free to choose the position of the first point, and then determine the subsequent $2r$ points based on the optimal spacing of \mathbf{x}^* . For example, given any specific $\theta \in \mathbb{R}$, we can choose $s := \theta - x_0^*$, then

$$\mathbf{x}_{new}^* = \mathbf{x}^* + s\mathbf{1} = [x_0^* + s, x_1^* + s, \dots, x_{2r}^* + s]^\dagger \quad (111)$$

$$= [\theta, \theta + (x_1^* - x_0^*), \dots, \theta + (x_{2r}^* - x_0^*)]^\dagger \quad (112)$$

is another valid solution and preserve the minimization of the $\text{MSE}(\hat{\mathbf{z}}_{\mathbf{x}})$ in Eq. (34). Moreover, to obtain the formulation for $A_{\mathbf{x}_{new}^*}^{-1}$, we do not need to naively compute the inverse matrix again. The first claim in Lemma 1 shows that we only need to multiply the original inverse matrix $A_{\mathbf{x}^*}^{-1}$ by a simple block diagonal matrix E_s^{-1} that depends on the shift value s , whose diagonal blocks are rotation matrices B_i .

C.2 Observation II: unbiasedness of the approximated function

The second observation is about the approximated function

$$\hat{f}(x) := \frac{1}{\sqrt{2}}\hat{a}_0 + \sum_{k=1}^r [\hat{a}_k \cos(\Omega_k x) + \hat{b}_k \sin(\Omega_k x)], \quad (113)$$

which can be fully processed on a classical computer once we have obtained the estimated coefficients $\hat{\mathbf{z}}_{\mathbf{x}}$. Let us define the vector

$$\mathbf{t}(x) := [1/\sqrt{2}, \cos(\Omega_1 x), \sin(\Omega_1 x), \dots, \cos(\Omega_r x), \sin(\Omega_r x)]^\dagger \in \mathbb{R}^n. \quad (114)$$

Then, $\hat{f}(x)$ can be expressed as

$$\hat{f}(x) = \mathbf{t}(x)^\dagger \hat{\mathbf{z}}_{\mathbf{x}}. \quad (115)$$

Due to the normal distribution properties of the random vector $\hat{\mathbf{z}}_{\mathbf{x}}$, $\hat{f}(x)$ itself also follows a normal distribution, with expectation

$$\mathbb{E}[\hat{f}(x)] = \mathbf{t}(x)^\dagger \mathbb{E}[\hat{\mathbf{z}}_{\mathbf{x}}] = \mathbf{t}(x)^\dagger \mathbf{z} = f(x). \quad (116)$$

So, $\hat{f}(x)$ provides unbiased estimates of the true evaluation $f(x)$ at any $x \in \mathbb{R}$, regardless of the interpolation nodes \mathbf{x} . Furthermore, as shown in Lemma 11 of Appendix D.5, the variance can be computed as

$$\text{Var}[\hat{f}(x)] = \mathbf{t}(x)^\dagger \text{VAR}[\hat{\mathbf{z}}_{\mathbf{x}}] \mathbf{t}(x) = \langle \text{VAR}[\hat{\mathbf{z}}_{\mathbf{x}}], \mathbf{t}(x) \mathbf{t}(x)^\dagger \rangle. \quad (117)$$

Clearly, this variance depends on both the interpolation nodes \mathbf{x} and the univariate x . A natural idea is to consider a global variance quantity that eliminates the dependence on a specific univariate x . For example, assuming f and \hat{f} have a period $T > 0$ (usually 2π), we can use the following quantity:

$$h(\mathbf{x}) := \frac{1}{T} \int_0^T \text{Var}[\hat{f}(x)] dx = \langle \text{VAR}[\hat{\mathbf{z}}_{\mathbf{x}}], \frac{1}{T} \int_0^T \mathbf{t}(x)\mathbf{t}(x)^\dagger dx \rangle, \quad (118)$$

to evaluate the quality of the interpolation nodes. Minimizing $h(\mathbf{x})$ could give us a better overall estimate of f . However, in general, if the frequencies Ω_k 's are not assumed to be rational or integer, then f or \hat{f} might not have a period (e.g., $\sin(x) + \sin(\pi x)$). If the integration interval in Eq. (118) is the entire \mathbb{R} , then $h(\mathbf{x})$ would be difficult to handle. Fortunately, in the next section, we will consider equidistant frequencies ($\forall \Omega_k = k$), which will make $h(\mathbf{x})$ easier to handle. Here, for general frequencies, we can still provide an upper bound for the variance, i.e., the MSE itself:

$$\text{Var}[\hat{f}(x)] = \sigma^2 \langle [A_{\mathbf{x}}^\dagger A_{\mathbf{x}}]^{-1}, \mathbf{t}(x)\mathbf{t}(x)^\dagger \rangle = \sigma^2 \|(A_{\mathbf{x}}^{-1})^\dagger \mathbf{t}(x)\|_F^2 \quad (119)$$

$$\leq \sigma^2 \|(A_{\mathbf{x}}^{-1})^\dagger\|_F^2 \|\mathbf{t}(x)\|^2 = \frac{n}{2} \sigma^2 \|A_{\mathbf{x}}^{-1}\|_F^2 = \frac{n}{2} \text{MSE}(\hat{\mathbf{z}}_{\mathbf{x}}). \quad (120)$$

Thus, the optimal \mathbf{x}^* under the criterion of Eq. (34) indeed ensures that the overall variance of the approximation \hat{f} is controlled.

D Proofs: Optimality of $\frac{2\pi}{n}$ -equidistant interpolation nodes

In Section 4, we asserted that $\frac{2\pi}{n}$ -equidistant interpolation nodes are optimal from three perspectives, as formalized in Theorems 1, 2, and 3. The purpose of this appendix is to prove these three theorems. We begin by establishing several auxiliary results.

D.1 Auxiliary results for Vandermonde matrix

Lemma 2. *Let $n \geq 2$ be an integer, and let m be any nonzero integer such that $-n < m < n$. Consider the n -th roots of unity (the solutions to the equation $z^n = 1$) $\omega_k = e^{2\pi i \frac{k}{n}}$ for $k = 0, 1, \dots, n-1$. Then,*

$$\sum_{k=0}^{n-1} \omega_k^m = 0. \quad (121)$$

Proof. We need to show $S := \sum_{k=0}^{n-1} e^{2\pi i \frac{mk}{n}} = 0$. This sum is a geometric series with the common ratio $q := e^{2\pi i \frac{m}{n}} \neq 1$ since m is a nonzero integer and $-n < m < n$. Then,

$$S = \sum_{k=0}^{n-1} q^k = \frac{1 - q^n}{1 - q}. \quad (122)$$

Since $q^n = (e^{2\pi i \frac{m}{n}})^n = e^{2\pi i m} = 1$, we have $S = 0$. \square

Lemma 3. *Let $n \geq 2$ be an integer. Consider the n -th roots of unity $\omega_k = e^{2\pi i \frac{k}{n}}$ for $k = 0, 1, \dots, n-1$. Then, for any pair k, j such that $k < j$, and $k, j = 0, 1, \dots, n-1$, we have*

$$1 + \frac{\omega_k}{\omega_j} + \left(\frac{\omega_k}{\omega_j}\right)^2 + \dots + \left(\frac{\omega_k}{\omega_j}\right)^{n-1} = 0. \quad (123)$$

Proof. Let ω be an arbitrary n -th root of unity and $\omega \neq 1$. Then, $\omega^n = 1$. Note that

$$(\omega - 1)(\omega^{n-1} + \omega^{n-2} + \dots + 1) = \omega^n - 1 = 0. \quad (124)$$

Since $\omega - 1 \neq 0$, we conclude that

$$1 + \omega + \omega^2 + \dots + \omega^{n-1} = 0. \quad (125)$$

Given $k < j$, and $k, j = 0, 1, \dots, n-1$, then

$$\frac{\omega_k}{\omega_j} = \frac{e^{2\pi i \frac{k}{n}}}{e^{2\pi i \frac{j}{n}}} = e^{2\pi i \frac{k-j}{n}} = e^{2\pi i \frac{n+k-j}{n}}. \quad (126)$$

Note that all possible values of $n+k-j$ are $1, 2, \dots, n-1$, except for 0 and n . Therefore, $\frac{\omega_k}{\omega_j}$ is again one of the n -th roots of unity but is not equal to one. Applying Eq. (125) completes the lemma. \square

Lemma 4. *Let $n \geq 2$ be an integer. Consider the n -th roots of unity $\omega_k = e^{2\pi i \frac{k}{n}}$ for $k = 0, 1, \dots, n-1$. Consider the Vandermonde matrix*

$$V := \begin{bmatrix} 1 & \omega_0 & \omega_0^2 & \cdots & \omega_0^{n-1} \\ 1 & \omega_1 & \omega_1^2 & \cdots & \omega_1^{n-1} \\ \vdots & \vdots & \vdots & \ddots & \vdots \\ 1 & \omega_{n-1} & \omega_{n-1}^2 & \cdots & \omega_{n-1}^{n-1} \end{bmatrix} \in \mathbb{C}^{n \times n}. \quad (127)$$

Then, $V^\dagger V = VV^\dagger = nI$.

Proof. First, consider the product

$$V^\dagger V = \begin{bmatrix} 1 & 1 & \cdots & 1 \\ \omega_0^{-1} & \omega_1^{-1} & \cdots & \omega_{n-1}^{-1} \\ \omega_0^{-2} & \omega_1^{-2} & \cdots & \omega_{n-1}^{-2} \\ \vdots & \vdots & \ddots & \vdots \\ \omega_0^{-(n-1)} & \omega_1^{-(n-1)} & \cdots & \omega_{n-1}^{-(n-1)} \end{bmatrix} \begin{bmatrix} 1 & \omega_0 & \omega_0^2 & \cdots & \omega_0^{n-1} \\ 1 & \omega_1 & \omega_1^2 & \cdots & \omega_1^{n-1} \\ \vdots & \vdots & \vdots & \ddots & \vdots \\ 1 & \omega_{n-1} & \omega_{n-1}^2 & \cdots & \omega_{n-1}^{n-1} \end{bmatrix}. \quad (128)$$

For indices $j, l = 1, \dots, n$, the component of $V^\dagger V$ is

$$[V^\dagger V]_{jl} = \sum_{k=0}^{n-1} \omega_k^{l-j}. \quad (129)$$

If $j = l$, then $[V^\dagger V]_{jj} = \sum_{k=0}^{n-1} \omega_k^0 = n$. Consider $j \neq l$. Note that all possible values of $l-j$ are $\pm 1, \pm 2, \dots, \pm(n-1)$. By Lemma 2, we have $[V^\dagger V]_{jl} = 0$. Thus, $V^\dagger V = nI$. Now consider the product

$$VV^\dagger = \begin{bmatrix} 1 & \omega_0 & \omega_0^2 & \cdots & \omega_0^{n-1} \\ 1 & \omega_1 & \omega_1^2 & \cdots & \omega_1^{n-1} \\ \vdots & \vdots & \vdots & \ddots & \vdots \\ 1 & \omega_{n-1} & \omega_{n-1}^2 & \cdots & \omega_{n-1}^{n-1} \end{bmatrix} \begin{bmatrix} 1 & 1 & \cdots & 1 \\ \omega_0^{-1} & \omega_1^{-1} & \cdots & \omega_{n-1}^{-1} \\ \omega_0^{-2} & \omega_1^{-2} & \cdots & \omega_{n-1}^{-2} \\ \vdots & \vdots & \ddots & \vdots \\ \omega_0^{-(n-1)} & \omega_1^{-(n-1)} & \cdots & \omega_{n-1}^{-(n-1)} \end{bmatrix}. \quad (130)$$

For indices $j, l = 1, \dots, n$, the component of VV^\dagger is

$$[VV^\dagger]_{jl} = \sum_{k=0}^{n-1} \left(\frac{\omega_j}{\omega_l} \right)^k. \quad (131)$$

If $j = l$, then $[VV^\dagger]_{jj} = \sum_{k=0}^{n-1} 1^k = n$. For $j \neq l$ and $j < l$, by Lemma 3, the elements above the diagonal are zeros. By symmetry, we have $VV^\dagger = nI$. \square

D.2 Other auxiliary results

Let S_{++}^n denote the set of $n \times n$ symmetric positive definite matrices. The following two properties about positive definite matrices can be found in many matrix textbooks.

Lemma 5. *For any $X \in S_{++}^n$, we have the inequality $\text{tr}(X^{-1}) \geq \frac{n^2}{\text{tr}(X)}$. The equality holds if and only if $X = \lambda I$ for some $\lambda > 0$.*

Lemma 6. For any $X \in S_{++}^n$, we have $(X^{-1})_{ii}X_{ii} \geq 1$ for all $i = 1, \dots, n$

Lemma 7. For $x_i > 0, \forall i = 1, \dots, n$, we have $(\sum_{i=1}^n x_i) \left(\sum_{i=1}^n \frac{1}{x_i} \right) \geq n^2$, with equality holding if and only if all x_i are equal.

Proof. By Cauchy–Schwarz inequality, we have

$$\left(\sum_{i=1}^n (\sqrt{x_i})^2 \right) \left(\sum_{i=1}^n \left(\frac{1}{\sqrt{x_i}} \right)^2 \right) \geq \left(\sum_{i=1}^n \left(\sqrt{x_i} \cdot \frac{1}{\sqrt{x_i}} \right) \right)^2 = n^2. \quad (132)$$

Equality holds if and only if there exists a constant $\lambda > 0$ such that $\lambda = \frac{\sqrt{x_i}}{\frac{1}{\sqrt{x_i}}} = x_i$, for all $i = 1, \dots, n$, i.e., when all x_i are equal. \square

Lemma 8. For $x_i > 0$ and $a_i > 0, \forall i = 1, \dots, n$, we have $(\sum_{i=1}^n a_i x_i) \left(\sum_{i=1}^n \frac{a_i}{x_i} \right) \geq (\sum_{i=1}^n a_i)^2$, with equality holding if and only if all x_i are equal.

Proof. By Cauchy–Schwarz inequality, we have

$$\left(\sum_{i=1}^n (\sqrt{a_i x_i})^2 \right) \left(\sum_{i=1}^n \left(\sqrt{\frac{a_i}{x_i}} \right)^2 \right) \geq \left(\sum_{i=1}^n \left(\sqrt{a_i x_i} \cdot \sqrt{\frac{a_i}{x_i}} \right) \right)^2 = \left(\sum_{i=1}^n a_i \right)^2. \quad (133)$$

Equality holds if and only if there exists a constant $\lambda > 0$ such that $\lambda = \frac{\sqrt{a_i x_i}}{\sqrt{\frac{a_i}{x_i}}} = x_i$, for all $i = 1, \dots, n$, i.e., when all x_i are equal. \square

D.3 Proof of Theorem 1

Proof of Theorem 1. We first demonstrate that $2\sigma^2$ is the (global) lower bound of cost function $\text{MSE}(\hat{\mathbf{z}}_{\mathbf{x}})$ in Eq. (40), and then we prove that this lower bound can be achieved when taking $\frac{2\pi}{n}$ -equidistant nodes defined in Eq. (39). These two steps will complete the proofs.

For any $\mathbf{x} \in \mathbb{R}^n$ with x_i distinct modulo 2π , consider the matrix $V_{\mathbf{x}}$ defined in Eq. (98). It is easy to see that $[V_{\mathbf{x}}^\dagger V_{\mathbf{x}}]_{kk} = n$ for all $k = 1, \dots, n$; thus, $\text{tr}(V_{\mathbf{x}}^\dagger V_{\mathbf{x}}) = n^2$. On the other hand, from the matrix relations Eq. (99) and $CC^\dagger = \frac{1}{2}I$ in Eq. (94), one has

$$\text{tr}(A_{\mathbf{x}}^\dagger A_{\mathbf{x}}) = \text{tr}(C^\dagger V_{\mathbf{x}}^\dagger D_{\mathbf{x}}^\dagger D_{\mathbf{x}} V_{\mathbf{x}} C) = \frac{1}{2} \text{tr}(V_{\mathbf{x}}^\dagger V_{\mathbf{x}}) = \frac{n^2}{2}. \quad (134)$$

By Lemma 5, we obtain

$$\text{MSE}(\hat{\mathbf{z}}_{\mathbf{x}}) = \sigma^2 \|A_{\mathbf{x}}^{-1}\|_F^2 = \sigma^2 \text{tr}([A_{\mathbf{x}}^\dagger A_{\mathbf{x}}]^{-1}) \geq \sigma^2 \frac{n^2}{\text{tr}(A_{\mathbf{x}}^\dagger A_{\mathbf{x}})} = \sigma^2 \frac{n^2}{\frac{n^2}{2}} = 2\sigma^2. \quad (135)$$

Hence, $2\sigma^2$ is a lower bound for $\text{MSE}(\hat{\mathbf{z}}_{\mathbf{x}})$ for all $\mathbf{x} \in \mathbb{R}^n$ with x_i distinct modulo 2π .

By Lemma 1, the value of $\text{MSE}(\hat{\mathbf{z}}_{\mathbf{x}})$ is invariant under any shift of \mathbf{x} . Therefore, it is sufficient to consider $\frac{2\pi}{n}$ -equidistant nodes \mathbf{x}^* without shift, i.e.,

$$x_k^* = \frac{2\pi}{n}k \quad \text{for } k = 0, 1, \dots, 2r. \quad (136)$$

This implies that $\omega_k \equiv e^{ix_k^*} = e^{2\pi i \frac{k}{n}}$ are the n -th roots of unity. In this case, by Lemma 4, we have $V_{\mathbf{x}^*}^\dagger V_{\mathbf{x}^*} = V_{\mathbf{x}^*} V_{\mathbf{x}^*}^\dagger = nI$. Hence,

$$A_{\mathbf{x}^*}^\dagger A_{\mathbf{x}^*} = C^\dagger V_{\mathbf{x}^*}^\dagger D_{\mathbf{x}^*}^\dagger D_{\mathbf{x}^*} V_{\mathbf{x}^*} C = C^\dagger V_{\mathbf{x}^*}^\dagger V_{\mathbf{x}^*} C = \frac{n}{2}I. \quad (137)$$

Then, $\text{MSE}(\hat{\mathbf{z}}_{\mathbf{x}^*}) = \sigma^2 \text{tr}([A_{\mathbf{x}^*}^\dagger A_{\mathbf{x}^*}]^{-1}) = \frac{2}{n} \sigma^2 \text{tr}(I) = 2\sigma^2$. Therefore, the lower bound $2\sigma^2$ is achieved at $\frac{2\pi}{n}$ -equidistant nodes \mathbf{x}^* . \square

D.4 Proof of Theorem 2

Given an arbitrary invertible complex matrix $X \in \mathbb{C}^{n \times n}$, the 2-norm condition numbers defined as

$$\kappa_2(X) := \|X\|_2 \|X^{-1}\|_2 = \frac{\sigma_{\max}(X)}{\sigma_{\min}(X)} \geq 1. \quad (138)$$

where $\|X\|_2$ is spectral norm, and $\sigma_{\max}(X)$ ($\sigma_{\min}(X)$) is the largest (smallest) singular value of X . The lower bound 1 is attained if and only if all singular values of X are equal. The next lemma implies that the condition number κ_2 is invariant under multiplication by a scaled unitary matrix.

Lemma 9. *Given any nonsingular complex matrix A and any complex matrix B with $B^\dagger B = \lambda I$ for some constant $\lambda > 0$, we have*

$$\kappa_2(AB) = \kappa_2(BA) = \kappa_2(A). \quad (139)$$

Proof. We have

$$\|BA\|_2^2 = \sup_{\mathbf{x} \in \mathbb{R}^n \setminus \{0\}} \frac{\langle BA\mathbf{x}, BA\mathbf{x} \rangle}{\|\mathbf{x}\|_2^2} = \sup_{\mathbf{x} \in \mathbb{R}^n \setminus \{0\}} \frac{\langle B^\dagger BA\mathbf{x}, A\mathbf{x} \rangle}{\|\mathbf{x}\|_2^2} \quad (140)$$

$$= \sup_{\mathbf{x} \in \mathbb{R}^n \setminus \{0\}} \frac{\lambda \langle A\mathbf{x}, A\mathbf{x} \rangle}{\|\mathbf{x}\|_2^2} = \lambda \|A\|_2^2, \quad (141)$$

and note that $B^{-1} = \frac{1}{\lambda} B^\dagger$, so

$$\|A^{-1}B^{-1}\|_2^2 = \sup_{\mathbf{x} \in \mathbb{R}^n \setminus \{0\}} \frac{\langle A^{-1}B^{-1}\mathbf{x}, A^{-1}B^{-1}\mathbf{x} \rangle}{\|\mathbf{x}\|_2^2} = \sup_{\mathbf{y} \in \mathbb{R}^n \setminus \{0\}} \frac{\langle A^{-1}\mathbf{y}, A^{-1}\mathbf{y} \rangle}{\|B\mathbf{y}\|_2^2} \quad (142)$$

$$= \sup_{\mathbf{y} \in \mathbb{R}^n \setminus \{0\}} \frac{\langle A^{-1}\mathbf{y}, A^{-1}\mathbf{y} \rangle}{\lambda \|\mathbf{y}\|_2^2} = \frac{1}{\lambda} \|A^{-1}\|_2^2. \quad (143)$$

Hence, we have

$$\kappa_2(BA) = \|BA\|_2 \|A^{-1}B^{-1}\|_2 = \|A\|_2 \|A^{-1}\|_2 = \kappa_2(A). \quad (144)$$

Similarly, one can show that $\kappa_2(AB) = \kappa_2(A)$. \square

Now we are ready to provide the proof of Theorem 2.

Proof of Theorem 2. We know that 1 is the global lower bound of the cost function $\kappa_2(A_{\mathbf{x}})$ in Eq. (43). Therefore, it remains to show that $\kappa_2(A_{\mathbf{x}^*}) = 1$ for the $\frac{2\pi}{n}$ -equidistant nodes \mathbf{x}^* defined in Eq. (39).

We first establish that the value of $\kappa_2(A_{\mathbf{x}})$ is invariant under any shift of \mathbf{x} . By Lemma 1, we know that for any shift s , we have

$$A_{\mathbf{x}+s\mathbf{1}} = A_{\mathbf{x}} E_s, \quad (145)$$

where $E_s = \text{Diag}(1, B_1, \dots, B_r) \in \mathbb{R}^{n \times n}$ and B_i are rotation matrices (hence unitary), as defined in Eq. (101). It is straightforward to verify that E_s is unitary. So, by applying Lemma 9, we obtain:

$$\kappa_2(A_{\mathbf{x}+s\mathbf{1}}) = \kappa_2(A_{\mathbf{x}}) \quad \text{for any shift value } s \in \mathbb{R}. \quad (146)$$

Thus, we can consider the $\frac{2\pi}{n}$ -equidistant nodes \mathbf{x}^* without any shift, i.e., $x_k^* = \frac{2\pi}{n}k$ for $k = 0, 1, \dots, 2r$. This implies that $\omega_k \equiv e^{ix_k^*} = e^{2\pi i \frac{k}{n}}$. In this case, by Lemma 4, we have $V_{\mathbf{x}^*}^\dagger V_{\mathbf{x}^*} = nI$.

Using the relations $A_{\mathbf{x}^*} = D_{\mathbf{x}^*} V_{\mathbf{x}^*} C$ from Eq. (99) and $C^\dagger C = \frac{1}{2}I$, we can apply Lemma 9 twice to obtain

$$\kappa_2(A_{\mathbf{x}^*}) = \kappa_2(V_{\mathbf{x}^*}). \quad (147)$$

Thus, it suffices to show that $\kappa_2(V_{\mathbf{x}^*}) = 1$. Since $V_{\mathbf{x}^*}^\dagger V_{\mathbf{x}^*} = nI$, we set $B = V_{\mathbf{x}^*}$ and $A = I$ in Lemma 9, yielding

$$\kappa_2(V_{\mathbf{x}^*}) = \kappa_2(I) = 1. \quad (148)$$

This completes the proof. \square

D.5 Proof of Theorem 3

Let us start with an auxiliary result in probability theory.

Lemma 10. *Consider the random vector \mathbf{x} with $\mathbb{E}[\mathbf{x}] = \mu$, $\text{VAR}[\mathbf{x}] = \Sigma$. If $A = yz^\dagger$ for some constant vectors y, z , then $\mathbb{E}[\mathbf{x}^\dagger A \mathbf{x}] = \mu^\dagger A \mu + \text{tr}(A \Sigma)$.*

Lemma 11. *For the d -th order derivative of $\hat{f}(x)$ in Eq. (113), i.e., $\hat{f}^{(d)}(x) = \mathbf{t}^{(d)}(x)^\dagger \hat{\mathbf{z}}_{\mathbf{x}}$ with $\mathbf{t}^{(d)}(x)$ given in Eq. (45). We have*

$$\text{Cov}[\hat{f}^{(d)}(x_1), \hat{f}^{(d)}(x_2)] = \mathbf{t}^{(d)}(x_1)^\dagger \text{VAR}[\hat{\mathbf{z}}_{\mathbf{x}}] \mathbf{t}^{(d)}(x_2), \quad \forall x_1, x_2 \in \mathbb{R}, \quad (149)$$

$$\text{Var}[\hat{f}^{(d)}(x)] = \mathbf{t}^{(d)}(x)^\dagger \text{VAR}[\hat{\mathbf{z}}_{\mathbf{x}}] \mathbf{t}^{(d)}(x), \quad \forall x \in \mathbb{R}. \quad (150)$$

Proof. To simplify notation, let $\hat{f}_1^{(d)} := \hat{f}^{(d)}(x_1)$ and $\hat{f}_2^{(d)} := \hat{f}^{(d)}(x_2)$; similarly, let $\mathbf{t}_1^{(d)} := \mathbf{t}^{(d)}(x_1)$ and $\mathbf{t}_2^{(d)} := \mathbf{t}^{(d)}(x_2)$. By Lemma 10, we can proceed as follows:

$$\text{Cov}[\hat{f}_1^{(d)}, \hat{f}_2^{(d)}] = \mathbb{E}[\hat{f}_1^{(d)} \hat{f}_2^{(d)}] - \mathbb{E}[\hat{f}_1^{(d)}] \mathbb{E}[\hat{f}_2^{(d)}] \quad (151)$$

$$= \mathbb{E}[\hat{\mathbf{z}}_{\mathbf{x}}^\dagger \mathbf{t}_1^{(d)} \mathbf{t}_2^{(d)T} \hat{\mathbf{z}}_{\mathbf{x}}] - \mathbf{t}_1^{(d)T} \mathbf{z} \cdot \mathbf{t}_2^{(d)T} \mathbf{z} \quad (152)$$

$$= \mathbf{z}^\dagger \mathbf{t}_1^{(d)} \mathbf{t}_2^{(d)T} \mathbf{z} + \text{tr} \left(\mathbf{t}_1^{(d)} \mathbf{t}_2^{(d)T} \text{VAR}[\hat{\mathbf{z}}_{\mathbf{x}}] \right) - \mathbf{z}^\dagger \mathbf{t}_1^{(d)} \cdot \mathbf{t}_2^{(d)T} \mathbf{z} \quad (153)$$

$$= \mathbf{t}_1^{(d)T} \text{VAR}[\hat{\mathbf{z}}_{\mathbf{x}}] \mathbf{t}_2^{(d)}, \quad (154)$$

which completes the proof. \square

Now we are ready to provide the proof of Theorem 3.

Proof of Theorem 3. For $d = 0$, as shown in Eq. (51), Theorem 3 reduces to Theorem 1, so we focus on the cases where $d \geq 1$. We first establish the lower bound of the cost function $h^{(d)}(\mathbf{x})$ in Eq. (50), and then prove that this lower bound is achieved when the $\frac{2\pi}{n}$ -equidistant nodes defined in Eq. (39) are used. These two steps complete the proof.

For $d \geq 1$, from Eq. (30) and Eq. (49), for all $\mathbf{x} \in \mathbb{R}^n$ (with distinct x_i modulo 2π), we have the following expression for $h^{(d)}(\mathbf{x})$:

$$h^{(d)}(\mathbf{x}) = \frac{1}{2} \langle \text{VAR}[\hat{\mathbf{z}}_{\mathbf{x}}], \text{Diag}(p) \rangle = \frac{1}{2} \sigma^2 \langle B^{-1}, \text{Diag}(p) \rangle, \quad (155)$$

where $p = [0, 1, 1, 2^{2d}, 2^{2d}, \dots, r^{2d}, r^{2d}]^\dagger \in \mathbb{R}^n$, and $B := A_{\mathbf{x}}^\dagger A_{\mathbf{x}} \in \mathbb{R}^{n \times n}$ is positive definite since $A_{\mathbf{x}}$ is invertible.

We then claim the following equality for any \mathbf{x} . Note that $n = 2r + 1$ and $p_1 = 0$, so we have

$$\sum_{i=1}^n p_i B_{ii} = \sum_{k=1}^r k^{2d} ([A_{\mathbf{x}}^\dagger A_{\mathbf{x}}]_{2k, 2k} + [A_{\mathbf{x}}^\dagger A_{\mathbf{x}}]_{2k+1, 2k+1}) \quad (156)$$

$$= \sum_{k=1}^r k^{2d} \left(\sum_{i=0}^{2r} [\cos^2(kx_i) + \sin^2(kx_i)] \right) \quad (\text{by definition of } A_{\mathbf{x}} \text{ in Eq. (23)}) \quad (157)$$

$$= \sum_{k=1}^r k^{2d} n. \quad (158)$$

Now, turn to Eq. (155), we have

$$h^{(d)}(\mathbf{x}) = \frac{1}{2}\sigma^2 \sum_{i=1}^n p_i [B^{-1}]_{ii} \geq \frac{1}{2}\sigma^2 \left(\sum_{i=1}^n p_i \right)^2 \left[\sum_{i=1}^n \frac{p_i}{[B^{-1}]_{ii}} \right]^{-1} \quad (\text{by Lemma 8}) \quad (159)$$

$$\geq \frac{1}{2}\sigma^2 \left(\sum_{i=1}^n p_i \right)^2 \left[\sum_{i=1}^n p_i B_{ii} \right]^{-1} \quad (\text{by Lemma 6}) \quad (160)$$

$$= \frac{1}{2}\sigma^2 \left(\sum_{i=1}^n p_i \right)^2 \left(n \sum_{k=1}^r k^{2d} \right)^{-1} \quad (\text{by equation Eq. (158)}) \quad (161)$$

$$= \frac{2\sigma^2}{n} \sum_{k=1}^r k^{2d}. \quad (162)$$

Thus, $\frac{2\sigma^2}{n} \sum_{k=1}^r k^{2d}$ is a lower bound for $h^{(d)}(\mathbf{x})$ for all \mathbf{x} .

Next, let us consider the $\frac{2\pi}{n}$ -equidistant nodes \mathbf{x}^* without shift, i.e., $x_k^* = \frac{2\pi}{n}k$ for $k = 0, 1, \dots, 2r$. By Lemma 4, we have

$$B = A_{\mathbf{x}^*}^\dagger A_{\mathbf{x}^*} = C^\dagger V_{\mathbf{x}^*}^\dagger D_{\mathbf{x}^*}^\dagger D_{\mathbf{x}^*} V_{\mathbf{x}^*} C = \frac{n}{2} I. \quad (163)$$

Thus, we obtain

$$h^{(d)}(\mathbf{x}^*) = \frac{1}{2}\sigma^2 \sum_{i=1}^n p_i (B^{-1})_{ii} = \frac{2\sigma^2}{n} \sum_{k=1}^r k^{2d}. \quad (164)$$

Therefore, the lower bound is achieved at \mathbf{x}^* without any shift.

Finally, it remains to establish that the value of $h^{(d)}(\mathbf{x})$ is invariant under any shift of \mathbf{x} , particularly for \mathbf{x}^* . By Lemma 1, we know that for any shift s , we have

$$A_{\mathbf{x}+s\mathbf{1}} = A_{\mathbf{x}} E_s, \quad (165)$$

where $E_s = \text{Diag}(1, B_1, \dots, B_r) \in \mathbb{R}^{n \times n}$, and $B_i \in \mathbb{R}^{2 \times 2}$ are rotation matrices, as defined in Eq. (101). Using this, we can express $h^{(d)}(\mathbf{x} + s\mathbf{1})$ as follows:

$$h^{(d)}(\mathbf{x} + s\mathbf{1}) = \frac{1}{2} \langle \text{VAR}[\hat{\mathbf{z}}_{\mathbf{x}+s\mathbf{1}}], \text{Diag}(p) \rangle \quad (166)$$

$$= \frac{1}{2}\sigma^2 \left\langle \left(A_{\mathbf{x}+s\mathbf{1}}^\dagger A_{\mathbf{x}+s\mathbf{1}} \right)^{-1}, \text{Diag}(p) \right\rangle \quad (167)$$

$$= \frac{1}{2}\sigma^2 \left\langle E_s^\dagger (A_{\mathbf{x}}^\dagger A_{\mathbf{x}})^{-1} E_s, \text{Diag}(p) \right\rangle \quad (168)$$

$$= \frac{1}{2} \langle \text{VAR}[\hat{\mathbf{z}}_{\mathbf{x}}], E_s \text{Diag}(p) E_s^\dagger \rangle. \quad (169)$$

On the other hand, we know that $E_s^\dagger = \text{Diag}(1, B_1^\dagger, \dots, B_r^\dagger)$ and that

$$\text{Diag}(p) = \text{Diag}(0, I_2, 2^{2d} I_2, \dots, r^{2d} I_2), \quad (170)$$

where I_2 is the 2×2 identity matrix. Therefore, we have

$$E_s \text{Diag}(p) E_s^\dagger = \text{Diag}(0, B_1 I_2 B_1^\dagger, 2^{2d} B_2 I_2 B_2^\dagger, \dots, r^{2d} B_r I_2 B_r^\dagger) = \text{Diag}(p). \quad (171)$$

Substituting this result into the expression for $h^{(d)}(\mathbf{x} + s\mathbf{1})$, we obtain

$$h^{(d)}(\mathbf{x} + s\mathbf{1}) = \frac{1}{2} \langle \text{VAR}[\hat{\mathbf{z}}_{\mathbf{x}}], \text{Diag}(p) \rangle = h^{(d)}(\mathbf{x}). \quad (172)$$

Thus, we have shown that $h^{(d)}(\mathbf{x})$ is invariant under any shift of \mathbf{x} . This completes the proof of Theorem 3. \square

E Review of general parameter shift rule

Let us review the parameter shift rule (PSR) [20]. Consider the cost function $f(x)$ in Eq. (20) under equidistant frequency Assumption 2, i.e.,

$$f(x) = \frac{1}{\sqrt{2}}a_0 + \sum_{k=1}^r [a_k \cos(kx) + b_k \sin(kx)]. \quad (173)$$

The general parameter shift rule aims to compute the derivative of $f(x)$ by only using linear combination of function evaluations. That is given by

$$g(x) := \frac{df}{dx}(x) = \sum_{\mu=1}^{2r} \frac{(-1)^{\mu-1}}{4r \sin^2(\frac{1}{2}x_\mu)} f(x + x_\mu), \quad (174)$$

where $x_\mu = \frac{\pi}{2r} + (\mu - 1)\frac{\pi}{r}$ for $\mu = 1, 2, \dots, 2r$. Note that the coefficients preceding this linear combination are only related to r and are independent of a_k and b_k . For example, when $r = 1$, it reduces to

$$g(x) = \frac{1}{4 \sin^2(\frac{1}{2} \cdot \frac{1}{2}\pi)} f\left(x + \frac{1}{2}\pi\right) - \frac{1}{4 \sin^2(\frac{1}{2} \cdot \frac{3}{2}\pi)} f\left(x + \frac{3}{2}\pi\right) \quad (175)$$

$$= \frac{1}{2} \left(f\left(x + \frac{\pi}{2}\right) - f\left(x - \frac{\pi}{2}\right) \right). \quad (176)$$

In previous works [20], one might use the estimator

$$g_{\text{psr}}(x) := \sum_{\mu=1}^{2r} \frac{(-1)^{\mu-1}}{4r \sin^2(\frac{1}{2}x_\mu)} \tilde{f}(x + x_\mu), \quad (177)$$

to approximate $g(x)$. In numerical simulation experiments, the calculation of gradients required for RCD and SGD is based on the PSR presented here. To the best of our knowledge, for general non-equidistant frequency Ω_k , there is currently no explicit PSR of the same form as equation Eq. (174).

F Eigenvalue method of solving subproblem for equidistant frequencies

In each iteration of OICD for equidistant frequencies, we need to find the global minimizer of the trigonometric polynomial

$$f(x) = \frac{1}{\sqrt{2}}a_0 + \sum_{k=1}^r [a_k \cos(kx) + b_k \sin(kx)] \quad (178)$$

for $x \in [0, 2\pi]$ (here, we omit the hat symbol on the coefficients). To achieve this, we first find all the real roots of its derivative

$$f'(x) = \sum_{k=1}^r [-a_k k \sin(kx) + b_k k \cos(kx)] = 0 \quad (179)$$

within the interval $[0, 2\pi]$. These roots correspond to the stationary points of $f(x)$. By evaluating $f(x)$ at these points, we can determine the global minimizer. Fortunately, [24, Theorem 2] provides a exact method for transforming the problem of finding the roots of Eq. (179) into an eigenvalue problem. We apply this method as follows.

Step 1: Note that $f'(x)$ has the same structure as $f(x)$, as it can be written as

$$f'(x) = \sum_{k=0}^r \tilde{a}_k \cos(kx) + \sum_{k=1}^r \tilde{b}_k \sin(kx) \quad (180)$$

where we define

$$\tilde{a}_k = \begin{cases} 0, & \text{for } k = 0 \\ b_k k, & \text{for } k = 1, 2, \dots, r \end{cases} \quad \text{and} \quad \tilde{b}_k = -a_k k, \text{ for } k = 1, 2, \dots, r. \quad (181)$$

It is assumed that both a_r and b_r are nonzero; otherwise, they should be removed, and r should be reduced.

Step 2: Define the coefficients h_j as

$$h_j = \begin{cases} \tilde{a}_{r-j} + i\tilde{b}_{r-j}, & j = 0, 1, \dots, r-1, \\ 2\tilde{a}_0, & j = r, \\ \tilde{a}_{j-r} - i\tilde{b}_{j-r}, & j = r+1, r+2, \dots, 2r. \end{cases} \quad (182)$$

Since $\tilde{a}_0 = 0$, it follows that $h_r = 0$.

Step 3: Next, define a $2r \times 2r$ matrix \mathbf{B} with entries B_{kj} as

$$B_{kj} = \begin{cases} \delta_{k,j-1}, & \text{for } k = 1, 2, \dots, 2r-1, \\ -\frac{h_{j-1}}{\tilde{a}_r - i\tilde{b}_r}, & \text{for } k = 2r, \end{cases} \quad (183)$$

where $\delta_{k,j-1}$ is the Kronecker delta function. For example, when $r = 2$, the matrix \mathbf{B} is explicitly

$$\mathbf{B} = \begin{bmatrix} 0 & 1 & 0 & 0 \\ 0 & 0 & 1 & 0 \\ 0 & 0 & 0 & 1 \\ -\frac{\tilde{a}_2 + i\tilde{b}_2}{\tilde{a}_2 - i\tilde{b}_2} & -\frac{\tilde{a}_1 + i\tilde{b}_1}{\tilde{a}_2 - i\tilde{b}_2} & 0 & -\frac{\tilde{a}_1 - i\tilde{b}_1}{\tilde{a}_2 - i\tilde{b}_2} \end{bmatrix}. \quad (184)$$

Note that \mathbf{B} has a significant sparse structure, with at most $4r - 2$ non-zero elements.

Step 4: Let the eigenvalues of \mathbf{B} be denoted by $z_t \in \mathbb{C}$. [24, Theorem 2] shows that the roots (which may be complex) of $f'(x) = 0$ are given by $x_t = -i \log(z_t)$ where the complex logarithm is defined as $\log(z) = \log|z| + i(\arg(z) + 2\pi m)$, $\forall m \in \mathbb{Z}$. Therefore, the final roots are

$$x_t = (\arg(z_t) + 2\pi m) - i \log|z_t|, \quad t = 1, 2, \dots, 2r, \quad \forall m \in \mathbb{Z}. \quad (185)$$

Since we are only interested in the real roots of $f'(x)$, these real roots correspond to the eigenvalues z_t lying on the unit circle. This simplifies to

$$x_t = \arg(z_t) + 2\pi m, \quad \text{when } |z_t| = 1. \quad (186)$$

By taking x_k modulo 2π , the final real roots can be obtained.

Step 5: The global minimizer is the value of x_t that yields the smallest $f(x)$ among these points.

This method uses the inherent properties of trigonometric polynomials to transform the problem of finding the global minimizer of $f(x)$ into an equivalent problem of determining all eigenvalues with modulus equal to 1 of a sparse non-Hermitian matrix \mathbf{B} . Compared to directly using global optimization solvers (e.g., differential evolution), which are typically heuristic algorithms, this eigenvalue approach guarantees the identification of the global minimum, thereby avoiding the risk of getting trapped in local minima. Although eigenvalue problems may appear complex, in practical applications, the integer r is usually small, making it feasible to solve the eigenvalues of small matrices both efficiently and accurately.

G Quantum circuits in numerical simulation

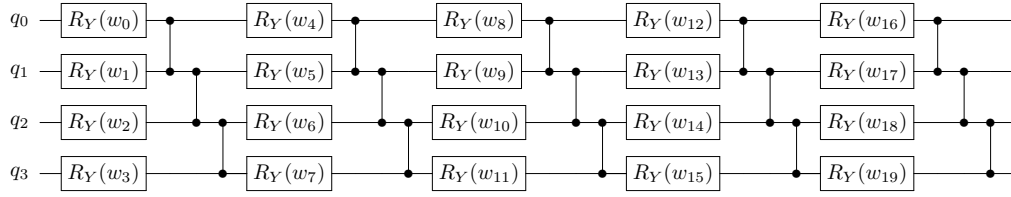


Figure 7: The HEA quantum circuit for the maxcut problem with $N = 4$ and $p = 5$.

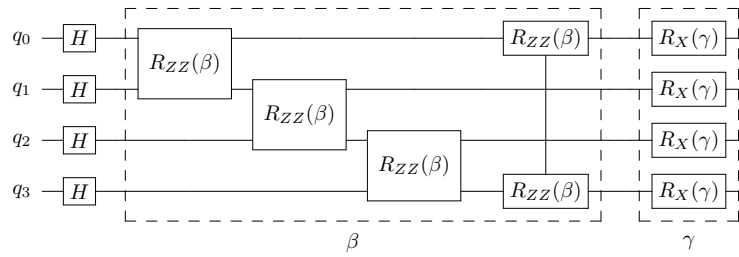


Figure 8: The HVA quantum circuit for the TFIM model with $N = 4$ and $p = 1$.

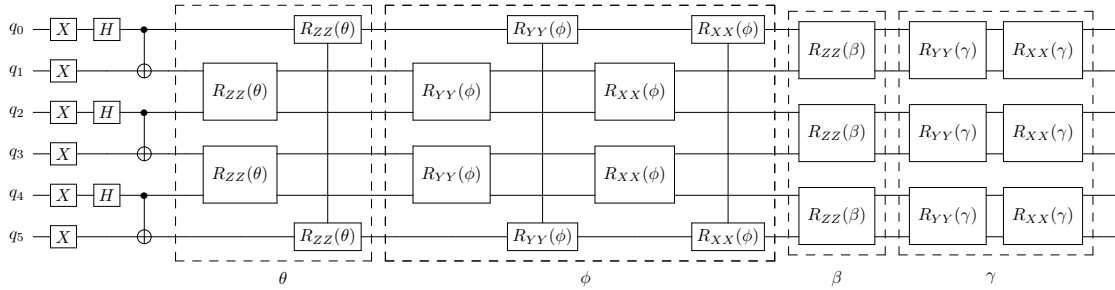


Figure 9: The HVA quantum circuit for the XXZ model with $N = 6$ and $p = 1$.